Substantial Cloud Brightening from Shipping in Subtropical Low Clouds

Michael S. Diamond[1,2], Hannah M. Director[3,2], Ryan Eastman[1], Anna Possner[4], Robert Wood[1]

[1]Department of Atmospheric Sciences, University of Washington, Seattle, USA.

[2]Program on Climate Change, University of Washington, Seattle, USA.

[3]Department of Statistics, University of Washington, Seattle, USA.

[4]Institute for Atmosphere and Environmental Sciences, Goethe University in Frankfurt, Germany.

Corresponding author: Michael S. Diamond (diamond2@uw.edu)

Key Points:

- Observations show for the first time that ship emissions induce a climate-scale cloud brightening effect in SE Atlantic stratocumulus deck
- Brightening is dominated by an increase in the number of cloud droplets, with small or countervailing adjustments in liquid water path
- Observationally-informed global effective radiative forcing in low clouds is calculated as -0.62 W/m^2 (-1.23 to -0.08 W/m^2)

Abstract

The influence of aerosol particles on cloud reflectivity remains one of the largest sources of uncertainty in our understanding anthropogenic climate change. Commercial shipping constitutes a large and concentrated aerosol perturbation in a meteorological regime where clouds have a disproportionally large effect on climate. Yet, to date, studies have been unable to detect climatologically-relevant cloud radiative effects from shipping, despite models indicating that the cloud response should produce a sizable negative radiative forcing (perturbation to Earth's energy balance).

We attribute a significant increase in cloud reflectivity to enhanced cloud droplet number concentrations within a major shipping corridor in the southeast Atlantic. Prevailing winds constrain emissions around the corridor, which cuts through a climatically-important region of expansive low-cloud cover. We use universal kriging, a classic geostatistical method, to estimate what cloud properties would have been in the absence of shipping. In the morning, cloud brightening is consistent with changes in microphysics alone, whereas in the afternoon, increases in cloud brightness from microphysical changes are offset by decreases in the total amount of cloud water. We find a radiative forcing in the southeast Atlantic shipping corridor two orders of magnitude greater than previous observational estimates. Approximately five years of data are required to identify a clear signal.

Extrapolating our results globally, we calculate an effective radiative forcing due to aerosol-cloud interactions in low clouds of -0.62 W/m^2 (-1.23 to -0.08 W/m^2). The unique setup in the southeast Atlantic could be an ideal test for the representation of aerosol-cloud interactions in climate models.

Plain Language Summary

One of the biggest challenges in quantifying the human influence on Earth's climate is understanding how small airborne particles ("aerosol") influence cloud properties. Increasing the amount of aerosol particles increases the brightness of low-lying clouds, exerting a cooling effect on the climate that partially offsets some of the warming caused by increasing greenhouse gas concentrations. Ship tracks, or lines of cloud changes caused by the pollution from individual ships, have long been studied as a prime example of these cloud-aerosol interactions in action. Mysteriously, however, previous attempts to measure ship tracks globally found small effects, even though climate models predict the effect should be much larger. We analyze a shipping corridor in the southeast Atlantic where the winds blow in such a way that the ships' pollution remains constrained around the corridor. This allows us to estimate what the clouds in the shipping corridor would look like without the effects of ships by using the properties of nearby, non-shipping-affected clouds. For the first time, we observe a substantial increase in cloud brightness caused by shipping on a regional scale. We suggest that the southeast Atlantic shipping corridor can be an ideal test of aerosol-cloud interactions in climate models.

1 Introduction: Tracks without a trace?

For decades, ships burning high-sulfur-content fuels have crossed the world's oceans, emitting airborne particles (aerosol) and aerosol-precursor gases in regions with relatively low levels of natural aerosol (Capaldo, Corbett, Kasibhatla, Fischbeck, & Pandis, 1999; Eyring et al., 2010). Changing cloud reflectivity due to interactions with aerosol particles has long been a major driver of uncertainty in assessments of present and future anthropogenic impacts on

Earth's climate (Andreae, Jones, & Cox, 2005; Myhre et al., 2013). Over the relatively dark oceans, changes in cloud brightness can have a disproportionally large impact on climate. Marine clouds, such as the subtropical stratocumulus that cover much of the low-latitude oceans, are also particularly sensitive to increases in aerosol concentrations as background aerosol levels are much lower over the oceans than over land (Oreopoulos & Platnick, 2008). To date, however, studies using satellite remote sensing have been unable to determine whether shipping emissions have a discernable, climatically-relevant impact on cloud-radiative properties (Peters, Quaas, & Graßl, 2011; Schreier, Mannstein, Eyring, & Bovensmann, 2007). This is surprising, as global climate models indicate cloud responses to shipping emissions should produce a substantial radiative effect (Capaldo et al., 1999; Lauer, Eyring, Hendricks, Jöckel, & Lohmann, 2007; Partanen et al., 2013; Peters, Quaas, Stier, & Graßl, 2014; Righi et al., 2011; Sofiev et al., 2018).

Ship tracks, or trails of cloud perturbations associated with emissions from individual ships, have been studied since the mid-1960s. Multiple hypotheses, such as that the tracks were aircraft contrails or even secret missile tests, were considered before they were correctly identified as resulting from ships traveling through conditions of shallow, cloudy marine boundary layers (MBLs) with low background aerosol levels (Conover, 1966; Twomey, Howell, & Wojciechowski, 1968). As aerosol concentrations increase (as happens when ships emit carbonaceous particles directly and the sulfur dioxide produced by burning shipping fuel is oxidized to create sulfate), more cloud condensation nuclei are available to form cloud droplets (Capaldo et al., 1999; Hobbs et al., 2000). Assuming the amount of liquid water in the clouds remains constant, this increases cloud droplet number concentration (N_d) and decreases the effective radius (r_e) of the droplets, resulting in more reflective clouds in what is known as the Twomey effect (Twomey, 1974, 1977). In the 1980s and 1990s, satellite (Coakley, Bernstein, & Durkee, 1987) and aircraft (Durkee, Chartier, et al., 2000; Durkee, Noone, et al., 2000; Radke, Coakley, & King, 1989) measurements confirmed that cloud condensation nuclei from shipping emissions increases N_d and decreases r_e, leading to the expected increase in cloud optical thickness (τ), a measure of cloud brightness.

Rapid adjustments in cloud macrophysics can either enhance or counteract the microphysical effect on cloud brightness. Initial ship track studies seemed to suggest that the liquid water path (LWP), or total amount of condensate, increased in ship tracks because shifting the droplet size distribution to smaller radii can reduce the loss of water from drizzle (Albrecht, 1989). However, later analyses (Ackerman et al., 2000; Chen et al., 2012; Coakley & Walsh, 2002) demonstrated that this is not always the case: cloudiness can also be reduced as increasing the cloud droplet number concentration enhances the cloud top entrainment of dry air, drying and deepening the MBL (Ackerman, Kirkpatrick, Stevens, & Toon, 2004; Bretherton, Blossey, & Uchida, 2007; Seifert, Heus, Pincus, & Stevens, 2015; Wood, 2007).

Although ship tracks have provided invaluable testbeds for aerosol-cloud interaction (ACI) hypotheses, observations have thus far suggested their overall climatic importance to be rather limited (Schreier et al., 2007). This may be due to undercounting, as clearly visible ship tracks are relatively rare (Gryspeerdt, Smith, O'Keeffe, Christensen, & Goldsworth, 2019). Hundreds or thousands (Campmany, Grainger, Dean, & Sayer, 2009; Toll, Christensen, Gassó, & Bellouin, 2017) have been identified by satellite per year even though there are on order 100,000 ships in the global fleet (Eyring et al., 2010). However, high-resolution model results suggest there can be radiatively-important impacts even when a clear ship track is not easily discernible (Possner, Wang, Wood, Caldeira, & Ackerman, 2018). In an attempt to capture

shipping's effect more holistically, one study looked for noticeable changes in cloud properties upwind or downwind of shipping corridors by following near-surface air mass trajectories that crossed these corridors, yet no unambiguous cloud micro- or macrophysical changes were detected (Peters et al., 2011).

Whereas observations show a small or unclear impact of shipping on global ACI, climate models (Capaldo et al., 1999; Lauer et al., 2007; Partanen et al., 2013; Peters et al., 2014; Righi et al., 2011; Sofiev et al., 2018) have produced substantial radiative forcings (energy imbalances) ranging from -0.06 to -0.6 W/m^2. A model known to have sizable shipping ACI effects was sampled using the aforementioned trajectory technique but also could not produce a clear signal, demonstrating that detection is hampered by the high meteorological variability of tropical low cloud properties and the lack of knowledge of what cloud properties would be in the absence of anthropogenic aerosol perturbations (Peters et al., 2014).

If the shipping signal is so elusive at regional and global scales, why not simply focus our efforts elsewhere? Numerous observational studies have found a correspondence between aerosol concentrations and cloud properties (Breon, Tanre, & Generoso, 2002; Martin, Johnson, & Spice, 1994; Rosenfeld et al., 2019). However, the confounding of aerosol effects and other meteorological variations that can significantly influence cloud properties remains a serious challenge for disentangling the magnitude of the aerosol effects alone (Adebiyi, Zuidema, & Abel, 2015; Gryspeerdt, Quaas, & Bellouin, 2016; Stevens & Feingold, 2009). For this reason, "natural experiments" in which there is a clear aerosol perturbation independent of meteorological influence, such as volcanic eruptions (Gryspeerdt, Goren, et al., 2019; Malavelle et al., 2017; McCoy & Hartmann, 2015; Toll et al., 2017; Toll, Christensen, Quaas, & Bellouin, 2019) and ship tracks (Chen et al., 2012; Gryspeerdt, Goren, et al., 2019; Toll et al., 2017; Toll et al., 2019), may represent our best opportunity for constraining ACI absent controlled experiments (Wood, Ackerman, Rasch, & Wanser, 2017).

2 Methods

2.1 General approach

A major shipping corridor in the southeast Atlantic was excluded from the previously discussed analyses because the vast majority of trajectories run parallel to the shipping corridor as opposed to crossing it. Indeed, MBL winds blow almost perfectly parallel to the shipping corridor as it cuts through an extensive stratocumulus cloud deck (Figure 1). These winds keep the emissions confined to a relatively narrow region surrounding the shipping corridor. Here, we take advantage of this confinement to estimate "counterfactual" fields (i.e., what would be expected in the absence of shipping perturbations) for the shipping corridor. The counterfactual fields are estimated with data from nearby, non-shipping-affected locations and covariate information using universal kriging (Zimmerman & Stein, 2010), a classical geostatistical method for spatial interpolation (see section 2.3 below). The counterfactual fields can then be compared to the "factual" fields of reanalysis or satellite data that are believed to be affected by shipping. This is conceptually akin to running a climate model with emissions turned off or on, and we refer to the kriged counterfactual fields as "NoShip" and the observation/reanalysis factual fields as "Ship" in an extension of this analogy. It should be emphasized that this method

analyzes the shipping corridor "top-down" as a whole rather than "bottom-up" via the aggregation of individual ship tracks.

We restrict our analysis to the 2003-2015 climatology (as that is the maximum time frame for which all of our data sources are available) and to the austral spring (September-October-November) season. Because the shipping lane spans a large geographical area with different meteorological regimes, we analyze a more equatorward "tropical" region (2-10ºS, 3ºE-13ºW) dominated by a trade cumulus cloud regime and the "subtropical" stratocumulus-dominated region (10-18ºS, 8ºE-8ºW) separately.

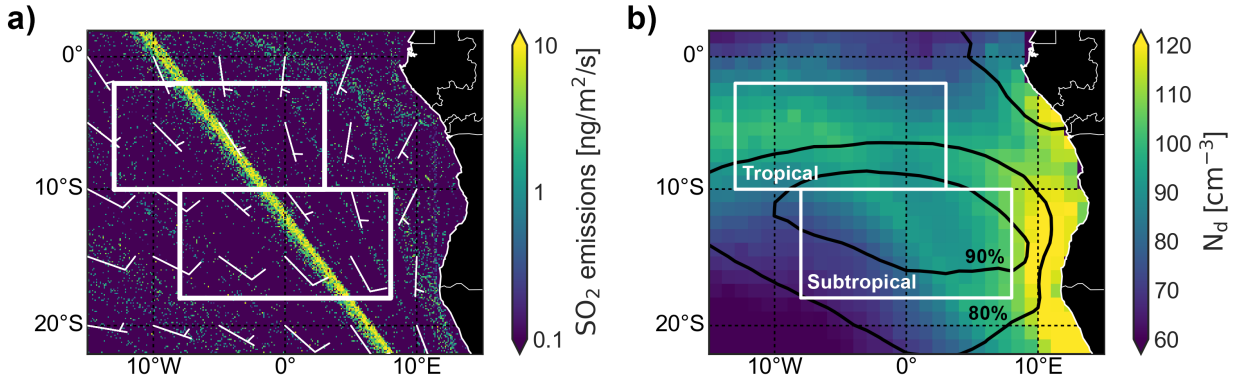

Figure 1. Austral spring shipping emissions, meteorology, and cloud properties in the southeast Atlantic. **a)** SO_2 emissions flux from international shipping (shading) and reanalysis winds at 1000 hPa (barbs; half line = 5 m/s, full line = 10 m/s, winds blow from tail to head) for austral spring (September-October-November). **b)** Satellite-derived cloud droplet number concentration (shading) and cloud fraction (contours of 80% and 90%) for austral spring. White boxes mark the tropical and subtropical regions of analysis.

2.2 Data

All variables analyzed in this study using the approach described in Section 2.1 are listed in Tables 1 and 2. We use cloud property retrievals from the Moderate Resolution Imaging Spectroradiometer (MODIS) instrument onboard the Terra and Aqua satellites, radiative fluxes from the Clouds and the Earth's Radiant Energy System (CERES) multi-sensor satellite products, and meteorological and aerosol properties from the Modern-Era Retrospective analysis for Research and Applications, Version 2 (MERRA-2).

SO_2 emissions from international shipping is taken from the Emissions Database for Global Atmospheric Research (EDGAR) for September, October, and November 2010 (Crippa et al., 2018). Sector-specific data broken down by month is only available for 2010. Because shipping emissions in the southeast Atlantic do not appear to undergo any major trends (Crippa et al., 2018), the 2010 values should be representative of all years in this study. SO_2 data are interpolated from the native 0.1º x 0.1º resolution to the 1.0º x 1.0º grid used for the monthly-average MODIS products discussed below.

Meteorological (1000 hPa horizontal winds and potential temperatures at 800 and 1000 hPa) and aerosol (surface sulfate and black carbon mass concentrations) data in this study come from MERRA-2 (Gelaro et al., 2017; Randles et al., 2017). Shipping emissions from the

EDGAR database are incorporated into the Goddard Chemistry, Aerosol, Radiation, and Transport model, which serves as the aerosol module for MERRA-2. MERRA-2 data are interpolated from the native 0.5º x 0.625º resolution to the 1.0º x 1.0º MODIS grid.

Cloud fraction (F_{cld}), effective radius, cloud optical thickness, and liquid water path are taken from the monthly Level-3, Collection-6 MODIS instrument products (Hubanks, Platnick, King, & Ridgway, 2019) for both the Terra (daytime satellite overpass time ~10:30 local, nighttime satellite overpass time ~22:30 local) and Aqua satellites (daytime satellite overpass time ~13:30 local, nighttime satellite overpass time ~01:30 local). Except for the cloud fraction fields, MODIS cloud properties are only available for the daytime overpass times. Cloud droplet number concentration is calculated using the retrievals of effective radius, cloud optical thickness, and cloud top temperature from MODIS/Aqua assuming a subadiabatic "Idealized Stratiform Boundary Layer Cloud" model (Bennartz & Rausch, 2017).

Total albedo, clear-sky albedo, and cloud albedo are calculated using the top-of-atmosphere (TOA) all-sky and clear-sky shortwave radiative fluxes, the incoming solar flux, and the cloud area fraction from the CERES Energy Balanced and Filled (EBAF) top-of-atmosphere Edition-4.0 data product (Loeb et al., 2018) for the daily-average values and from the CERES Synoptic Radiative Fluxes and Clouds (SYN) Edition-4a data product for hourly-resolved values. Cloud albedo (A_{cld}) is calculated from total albedo (A), clear-sky albedo (A_{clr}), and cloud fraction by rearranging the equation $A = F_{cld}A_{cld} + (1-F_{cld})A_{clr}$. Clear-sky downwelling shortwave radiative fluxes at the surface are taken from the CERES EBAF surface irradiance Edition-4.0 data product (Kato et al., 2018).

All the reanalysis and satellite data products discussed above cover the 2003-2015 time period. For all figures and tables, results are reported for analysis performed on the September-October-November 2003-2015 climatology unless otherwise noted.

Two additional data sources are utilized to calculate observationally-informed estimates of the global radiative forcing due to the Twomey effect alone (RF_{Twomey}) and the total effective radiative forcing due to aerosol-cloud interactions including cloud adjustments (ERF_{ACI}) in low clouds. Surface sulfate mass concentration data is analyzed from "historical" runs of those global climate models participating in the Coupled Model Intercomparison Project Phase 6 (CMIP6) that had posted relevant data as of November 14, 2019. More information about the models used and their ensemble members is provided in Supporting Information Table 1. The average sulfate mass concentration of the lowest model level for the first 15 years of the historical run (January 1850 to December 1864) is taken as the "pre-industrial" value and the corresponding average for the last 15 years (January 2000 to December 2014) is taken as the "present-day" value.

Radiative forcing estimates are calculated separately for "cumuliform-type" clouds (for which we consider our results from the tropical region to be representative) and "stratiform-type" clouds (for which we consider our results from the subtropical region to be representative). The Extended Edited Cloud Reports Archive (EECRA), which uses visual observer data from weather stations and ships that is reported in the World Meteorological Organization's (WMO) synoptic code (Eastman, Warren, & Hahn, 2011; Warren, Hahn, London, Chervin, & Jenne, 1986, 1988), is used to create cumuliform (F_{Cu}) and stratiform (F_{Sc}) cloud fractions. The cumuliform cloud fraction is created by aggregating observations of Types 1-2 (cumulus) and

Type 8 (cumulus under stratocumulus) whereas the stratiform cloud fraction is created by aggregating observations of Types 4-5 (stratocumulus), Type 6 (stratus), and Type 11 (fog) from between 06:00 and 18:00 local time for 1954-2008 (ocean observations) and 1971-2009 (land observations). Type 11 is not contained in the original WMO synoptic code and is processed specifically for the EECRA dataset. The exclusion of Type 3 (cumulonimbus without anvils), Type 7 (stratus and cumulus fractus of bad weather), and Type 9 (cumulonimbus with anvils) from our analysis should eliminate almost all observations coinciding with heavy precipitation.

The CMIP6 and EECRA data are interpolated or aggregated, respectively, to a common 5.0º x 5.0º grid. We require 20 valid observations per grid box to compute an average for the EECRA cloud fractions. Land boxes with multiple stations are averaged by first computing mean statistics for each station within the box; those means are then averaged (no weighting applied). Averages for boxes containing both land and ocean are calculated by computing an average for the land and ocean portions separately. Those separate averages are then weighted by land/ocean fraction in each grid box. Missing data is filled by setting the grid box average to zero for areas poleward of 67º (this mainly affects Greenland and Antarctica) and by averaging all neighboring valid grid box values otherwise (this mainly affects certain subtropical desert regions like the Sahara).

2.3 Universal kriging

Universal kriging is a classic geostatistical method (Zimmerman & Stein, 2010) designed to estimate some value at unknown spatial locations based partially on nearby observations of the same value. At each unknown location, the mean value is estimated from a regression model. Error, or noise, around all mean values is assumed to be spatially correlated. The correlation of the error between two values is further assumed to be a function only of the distance between locations, a property known as stationarity. We use the statistical package geoR (Ribeiro & Diggle, 2018) in R (R Core Team, 2019) for implementing this analysis.

Shipping-influenced grid boxes are identified by choosing the grid box at each latitude with the greatest SO_2 emissions from the EDGAR emissions database and the two neighboring grid boxes to the east and west. This results in five grid boxes identified as “shipping-affected” for each latitude in the two analysis boxes, for a total of 40 grid boxes per region. This extent was chosen to ensure that most of the area affected by the diffuse edges of the aerosol perturbation were categorized as shipping-influenced, while maintaining enough reference grid boxes to robustly fit the kriging model.

The mean value is obtained with linear regression using the possible covariates of latitude (lat), longitude (lon), their squares (lat^2 and lon^2), and their product (lat*lon) in addition to lower tropospheric stability (LTS; defined here as the potential temperature difference between 800 and 1000 hPa) and an “effective” measure of LTS (EffLTS) accounting for MBL advection:

$$\text{EffLTS} \equiv \text{LTS} - (1\ \text{day})\ \mathbf{u}\cdot\nabla(\text{LTS}),$$

where the zonal and meridional winds are taken from the 1000 hPa level. This second LTS measure was created to account for the fact that cloud cover is more strongly correlated with the LTS the MBL experienced 24-36 hours prior than with its instantaneous value (Klein, Hartmann,

& Norris, 1995; Mauger & Norris, 2010) — this effective LTS measure is essentially a Lagrangian adjustment to what is otherwise a fundamentally Eulerian analysis. Not all potential regressors are used to create each variable's mean function. To select an appropriate model, the Bayesian Information Criterion (BIC) is computed for all possible combinations of regressors and the combination that minimizes the BIC is selected. Supporting Information Tables S1 and S2 list the regressors used for each variable for the subtropical and tropical regions, respectively.

To ensure errors around the mean function are normally distributed (insofar as possible), some variables are transformed via the logarithm or logit function. Each variable's transformation, if any, is reported in Supporting Information Tables S2 and S3.

The stationary error term is estimated by fitting a parametric covariance model (here assumed to be exponential) to an empirical variogram, a plot of the squared difference between pairs of variables versus their distance, using weighted least squares. Binned empirical variograms and the fitted variograms are provided for the subtropical and tropical domains in Supporting Information Figures S1 and S2, respectively.

2.4 Significance testing

We perform three distinct tests of significance in this study: 1) the significance of individual grid boxes, 2) the significance of the field of grid boxes, and 3) the significance of the average Ship-NoShip difference within the core shipping lane.

For the first test, each grid box is considered to be individually significant if its factual (Ship) value is either above the 97.5th or below the 2.5th percentile of the distribution obtained via kriging for its counterfactual (NoShip) value. For the second test, we evaluate how extreme the number of individually significant grid boxes in the full region is compared to the number we would expect under the null hypothesis that the region is unaffected by shipping. Using the statistical model that kriging provides, we simulate 5,000 null fields for the full region. The p-value is the fraction of simulations that have a number of individually significant grid boxes equal to or greater than that of the factual case. By simulating full regions in addition to individual grid boxes, we account for the effect correlated error structures can have. Because we are testing multiple hypotheses, we apply a Benjamini-Hochberg adjustment (Benjamini & Hochberg, 1995) to this p-value to control the false discovery rate, or the proportion of false positives expected given the number of tests. Accounting for multiple testing meaningfully affects our results: both CERES EBAF total albedo and MODIS/Aqua liquid water path in the subtropical region would be considered field significant (at the standard 5% significance level) using the raw p-values but are not significant under the more stringent adjustment.

If a variable shows individual grid boxes both above and below the 95% confidence interval, field significance is assessed using the direction in which the majority of the individually significant grid boxes fall. The only variable that is assessed by our method to be field significant in which this situation arises is the MODIS/Aqua 13:30 local cloud fraction, in which 7 grid boxes lie above the 97.5th percentile and two grid boxes lie below the 2.5th percentile. Although the majority of the individually significant grid boxes show an increase in cloud fraction, the central tendency of the field is toward reductions in cloud fraction. While it is

possible that there are real cloud responses in this region that are subtler than our methods were designed to accommodate, we consider it more likely that this is a false positive.

For testing if the average Ship-NoShip difference is significant, we focus on the core of the shipping corridor, defined as grid boxes with SO_4 increases greater than 20%, rather than the more diffuse edges of the aerosol anomaly. We deem the average change to be significant if the resulting values are distinct from zero at the 95% confidence level. We estimate uncertainty as the spread in the factual-counterfactual (Ship-NoShip) differences for all 5,000 simulations from the statistical model obtained from kriging.

We place the greatest amount of confidence in the results that are both field significant and with average Ship-NoShip difference distinguishable from zero, such as those for N_d, effective radius, and cloud albedo in the subtropical region. Although some results — like those for cloud optical thickness from MODIS/Terra and liquid water path from MODIS/Aqua — are not field significant, we still have moderate confidence in their reliability given the consistency of the sign of their effect. We have low confidence that variables that are neither field significant nor with average Ship-NoShip difference distinguishable from zero are perturbed by the shipping effects and thus refrain from drawing strong conclusions about changes in these variables.

Table 1. Mean Ship values, absolute and relative Ship-NoShip differences, and adjusted p-values for field significance (p_{field}) for each variable for the subtropical domain. All values reported are averaged over the grid boxes with a relative increase in SO_4 exceeding 20%. 95% confidence intervals are indicated in parentheses. Variables that are both field significant at the 95% confidence level and have average Ship-NoShip differences that are significantly distinguishable from zero at the 95% confidence level are emboldened.

Variable	Units	Mean Ship value	Absolute Ship-NoShip difference	Relative Ship-NoShip difference (%)	p_{field}
MERRA-2					
Black carbon (BC)	**ng/kg**	**123.8**	**14.3 (12.3 to 16.3)**	**11.6 (10.0 to 13.2)**	**0.0**
Sulfate (SO_4)	**ng/kg**	**615**	**150 (136 to 165)**	**24.4 (22.1 to 26.8)**	**0.0**
MODIS/Terra					
Daytime cloud fraction ($F_{cld,1030}$)	%	88.09	0.05 (-0.27 to 0.40)	0.06 (-0.31 to 0.45)	1.0
Nighttime cloud fraction ($F_{cld,2230}$)	%	86.44	-0.28 (-0.64 to 0.08)	-0.32 (-0.74 to 0.09)	0.743
Effective radius (r_e)	**µm**	**10.83**	**-0.28 (-0.34 to -0.22)**	**-2.60 (-3.14 to -2.04)**	**0.0**
Cloud optical thickness (τ)	none	11.07	0.24 (0.10 to 0.37)	2.13 (0.93 to 3.35)	0.743
Liquid water path (LWP)	g/m^2	85.23	-0.48 (-1.57 to 0.60)	-0.57 (-1.85 to 0.71)	1.0
MODIS/Aqua					
Daytime cloud fraction ($F_{cld,1330}$)	%	91.30	0.16 (-0.23 to 0.57)	0.17 (-0.25 to 0.63)	1.0
Nighttime cloud fraction ($F_{cld,0130}$)	%	95.98	-0.03 (-0.29 to 0.23)	-0.04 (-0.30 to 0.24)	1.0
Cloud droplet number (N_d)	**cm^{-3}**	**93.25**	**4.87 (3.64 to 6.10)**	**5.22 (3.90 to 6.55)**	**0.0**
Effective radius (r_e)	**µm**	**11.41**	**-0.29 (-0.37 to -0.21)**	**-2.53 (-3.23 to -1.83)**	**0.0**
Cloud optical thickness (τ)	none	8.73	0.05 (-0.04 to 0.15)	0.57 (-0.50 to 1.67)	1.0
Liquid water path (LWP)	g/m^2	66.08	-1.32 (-2.15 to -0.49)	-2.00 (-3.25 to -0.74)	0.079
CERES EBAF					
Total albedo (A)	%	33.70	0.44 (0.20 to 0.68)	1.30 (0.59 to 2.01)	0.064
Cloud albedo (A_{cld})	**%**	**35.44**	**0.49 (0.28 to 0.70)**	**1.37 (0.79 to 1.96)**	**0.002**
Cloud fraction (F_{cld})	%	92.58	0.19 (-0.15 to 0.53)	0.20 (-0.16 to 0.57)	0.206
CERES SYN (09:30-11:30 UTC)					
Total albedo (A)	**%**	**31.70**	**0.52 (0.28 to 0.76)**	**1.63 (0.88 to 2.41)**	**0.002**
Cloud albedo (A_{cld})	**%**	**33.52**	**0.54 (0.33 to 0.75)**	**1.62 (0.99 to 2.25)**	**0.0**
Cloud fraction (F_{cld})	%	92.57	0.36 (-0.04 to 0.77)	0.39 (-0.05 to 0.83)	0.051
CERES SYN (12:30-14:30 UTC)					
Total albedo (A)	%	27.56	0.20 (-0.02 to 0.44)	0.74 (-0.08 to 1.60)	1.0
Cloud albedo (A_{cld})	%	30.11	0.24 (0.03 to 0.46)	0.81 (0.09 to 1.54)	0.435
Cloud fraction (F_{cld})	%	88.20	0.24 (-0.24 to 0.75)	0.27 (-0.27 to 0.85)	0.743

Table 2. Mean Ship values, absolute and relative Ship-NoShip differences and adjusted p-values for field significance (p_{field}) for each variable for the tropical domain. All values reported are averaged over the grid boxes with a relative increase in SO_4 exceeding 20%. 95% confidence intervals are indicated in parentheses. Variables that are both field significant at the 95% confidence level and have average Ship-NoShip differences that are significantly distinguishable from zero at the 95% confidence level are emboldened.

Variable	Units	Mean Ship value	Absolute Ship-NoShip difference	Relative Ship-NoShip difference (%)	p_{field}
MERRA-2					
Black carbon (BC)	**ng/kg**	**223.5**	**8.9 (5.9 to 11.8)**	**4.0 (2.6 to 5.3)**	**0.0**
Sulfate (SO_4)	**ng/kg**	**716**	**171 (160 to 181)**	**23.8 (22.4 to 25.2)**	**0.0**
MODIS/Terra					
Daytime cloud fraction ($F_{cld,1030}$)	%	74.51	0.74 (-0.04 to 1.56)	1.00 (-0.05 to 2.09)	0.121
Nighttime cloud fraction ($F_{cld,2230}$)	%	68.04	-0.17 (-1.12 to 0.78)	-0.25 (-1.64 to 1.15)	0.352
Effective radius (r_e)	**μm**	**11.25**	**-0.08 (-0.15 to -0.01)**	**-0.74 (-1.35 to -0.12)**	**0.047**
Cloud optical thickness (τ)	none	9.54	0.18 (-0.01 to 0.38)	1.94 (-0.13 to 3.98)	1.0
Liquid water path (LWP)	g/m^2	77.27	1.11 (-0.85 to 3.10)	1.44 (-1.10 to 4.02)	1.0
MODIS/Aqua					
Daytime cloud fraction ($F_{cld,1330}$)	%	74.02	-0.31 (-1.33 to 0.68)	-0.41 (-1.79 to 0.92)	0.026
Nighttime cloud fraction ($F_{cld,0130}$)	%	80.21	-0.34 (-1.30 to 0.65)	-0.42 (-1.62 to 0.81)	0.204
Cloud droplet number (N_d)	**cm^{-3}**	**95.15**	**2.05 (0.73 to 3.36)**	**2.15 (0.77 to 3.53)**	**0.026**
Effective radius (r_e)	μm	11.94	-0.07 (-0.17 to 0.04)	-0.56 (-1.43 to 0.33)	1.0
Cloud optical thickness (τ)	none	8.46	0.06 (-0.04 to 0.15)	0.66 (-0.50 to 1.83)	0.676
Liquid water path (LWP)	g/m^2	67.18	0.15 (-0.93 to 1.22)	0.23 (-1.38 to 1.82)	0.676
CERES EBAF					
Total albedo (A)	%	25.65	0.19 (-0.17 to 0.54)	0.75 (-0.65 to 2.11)	0.124
Cloud albedo (A_{cld})	%	30.79	0.20 (-0.13 to 0.54)	0.65 (-0.44 to 1.74)	0.352
Cloud fraction (F_{cld})	%	73.17	-0.56 (-1.46 to 0.33)	-0.77 (-1.99 to 0.45)	0.121
CERES SYN (09:30-11:30 UTC)					
Total albedo (A)	**%**	**25.08**	**0.39 (0.05 to 0.72)**	**1.54 (0.22 to 2.88)**	**0.015**
Cloud albedo (A_{cld})	%	30.45	0.37 (0.03 to 0.72)	1.22 (0.09 to 2.37)	0.352
Cloud fraction (F_{cld})	%	75.33	0.32 (-0.36 to 1.01)	0.43 (-0.48 to 1.34)	0.015
CERES SYN (12:30-14:30 UTC)					
Total albedo (A)	%	20.80	0.09 (-0.22 to 0.40)	0.43 (-1.07 to 1.93)	0.676
Cloud albedo (A_{cld})	%	26.86	0.07 (-0.13 to 0.26)	0.24 (-0.49 to 0.96)	0.124
Cloud fraction (F_{cld})	%	67.49	-0.32 (-1.45 to 0.87)	-0.47 (-2.15 to 1.29)	0.121

3 Cloud microphysical changes

Tables 1 and 2 contain our results for each variable analyzed for the subtropical and tropical regions, respectively.

Figure 2 shows the mean counterfactual NoShip estimate obtained from kriging and the factual Ship fields for three aerosol and cloud microphysical variables: surface sulfate mass concentrations (SO_4), cloud droplet number concentration, and effective radius (from MODIS/Aqua). Substantial differences between the observed Ship and mean NoShip estimate indicate an effect of shipping on the cloud properties.

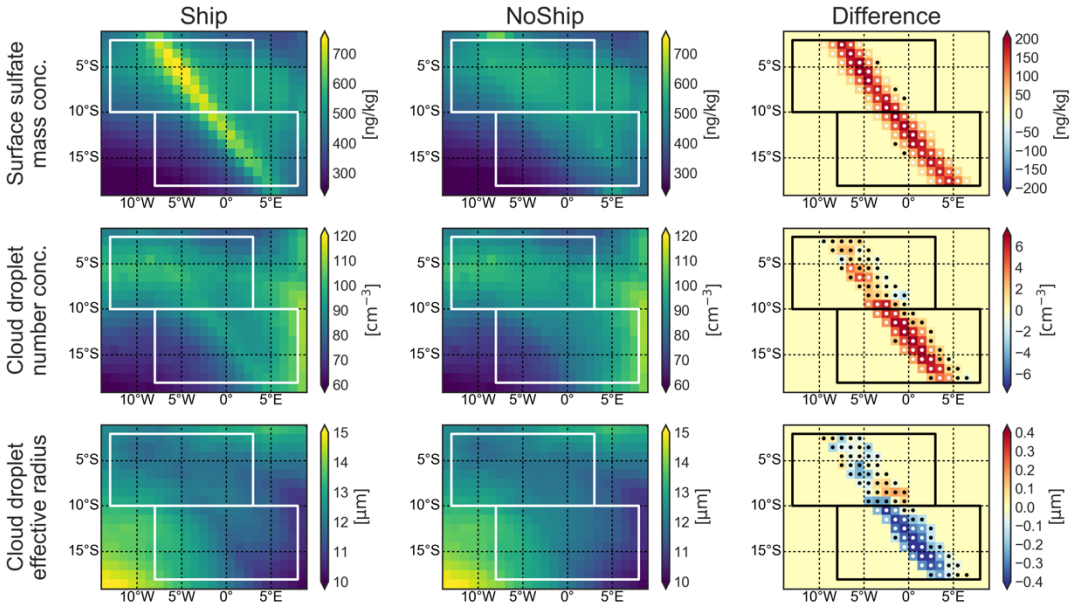

Figure 2. Ship, estimated mean NoShip, and their difference (columns) for SO_4, N_d, and r_e (rows). The effective radius values shown are from MODIS/Aqua. White (left and center) and black (right) boxes represent the two analysis regions. Shipping-affected grid boxes are marked by white dots when the Ship values are outside the 95% confidence interval of estimated NoShip values and by black dots otherwise.

Although the surface sulfate mass increases significantly in both the tropical and subtropical regions, only the latter region shows consistently significant changes in cloud microphysical properties. We therefore focus the bulk of our discussion on the subtropical region.

A commonly used metric (Feingold, Remer, Ramaprasad, & Kaufman, 2001; McComiskey et al., 2009; McCoy et al., 2017) for the strength of aerosol-cloud interactions, the ACI parameter, can be defined here as the fractional change in N_d per fractional change in sulfate mass, $\delta\ln(N_d)/\delta\ln(SO_4)$. In the subtropical region, an approximately 25% increase in SO_4 corresponds to an approximately 5% increase in N_d, resulting in an ACI parameter of 0.21 (95% confidence interval: 0.16 to 0.27). Estimating the ACI parameter with r_e instead of N_d, $\delta\ln(N_d)/\delta\ln(SO_4) \approx -3\ \delta\ln(r_e)/\delta\ln(SO_4)$, results in higher values of 0.31 (0.22 to 0.40) and 0.32 (0.25 to 0.39) for MODIS/Aqua and MODIS/Terra, respectively. However, this calculation assumes that liquid water path does not change, which is not necessarily true. The discrepancy

between ACI parameters estimated using N_d versus r_e is a cause for caution in interpreting r_e-derived ACI values when the liquid water path may also be changing.

Although no published Terra N_d product is currently available, the relative change in N_d can be estimated from the changes in r_e and liquid water path as $\delta N_d/N_d \approx \delta LWP/LWP - 3\delta r_e/r_e$. From this, δN_d is estimated as 7.2 cm^{-3} (5.1 to 9.3 cm^{-3}) in the morning. The ACI parameter calculated using the MODIS/Terra $\delta N_d/N_d$ is 0.30 (0.21 to 0.39). One physical explanation for larger cloud droplet number increases in the morning is that higher in-cloud supersaturations from stronger updrafts in the morning may activate a larger fraction of the shipping-generated aerosol particles, which tend to be quite small in diameter (Hobbs et al., 2000; Petzold et al., 2010).

4 Cloud macrophysical changes

Despite the clear increases in N_d, we do not find significant or consistent changes in cloud fraction (F_{cld}) in the daily average or at any particular time of day from either MODIS or CERES satellite retrieval products (Tables 1 and 2).

In the subtropical region, we find a decrease in liquid water path that is statistically distinguishable from zero in the afternoon. The larger decrease in liquid water path as the day progresses is consistent with previous modeling results (Sandu, Brenguier, Geoffroy, Thouron, & Masson, 2008) showing that the net sign of the cloud adjustments at night is sensitive to the competition between drizzle suppression and entrainment drying whereas during the day the enhanced entrainment effects dominate.

Afternoon heating of the marine boundary layer by black carbon, which is also emitted by ships, could also potentially lead to decreases in LWP. A diabatic heating rate is calculated for the absorption of black carbon throughout the depth of the marine boundary layer in the afternoon for the subtropical domain. An absorption coefficient (k_a) for the black carbon emitted by shipping is calculated by assuming a relatively high value for the mass absorption cross section of black carbon of 15 m^2/g and multiplying by the estimated increase in black carbon from Table 1 and the air density (ρ_a). The amount of incoming energy flux absorbed (dF) in an infinitesimal vertical layer (dz) of boundary layer air is given by Beer's Law as $dF = -k_a F\, dz$. Integrating over the depth of the marine boundary layer (h) and recognizing that $k_a h \ll 1$, the shortwave flux absorbed in the marine boundary layer (ΔF) can be expressed as $\Delta F = S k_a h$, where S is calculated as the top-of-atmosphere solar shortwave flux averaged around the Aqua overpass time over the subtropical domain (~1080 W/m^2). Using the top-of-atmosphere insolation should overestimate the shortwave flux available to be absorbed by neglecting scattering and absorption of sunlight by gases and particles above the MBL. The diabatic heating rate is then calculated as $dT/dt = (S k_a h)/(c_p \rho_a h)$, where c_p is the specific heat capacity of dry air. For our estimated values, the heating rate in the afternoon is only ~0.001 K/hour, which is negligible.

Cloud optical thickness is related to the effective droplet radius and liquid water path as $\tau \propto LWP\, r_e^{-1}$. Figure 3 decomposes the relative cloud optical thickness changes into components due to relative changes in LWP and r_e separately for the morning (Terra) and afternoon (Aqua);

$\delta\tau/\tau \approx \delta LWP/LWP - \delta r_e/r_e$. Probability densities are calculated from the 5,000 Ship-NoShip estimates for each variable via Gaussian kernel density estimation (KDE). The relative cloud optical thickness change calculated from the LWP and r_e components closely matches the relative change calculated directly from the Ship-NoShip differences.

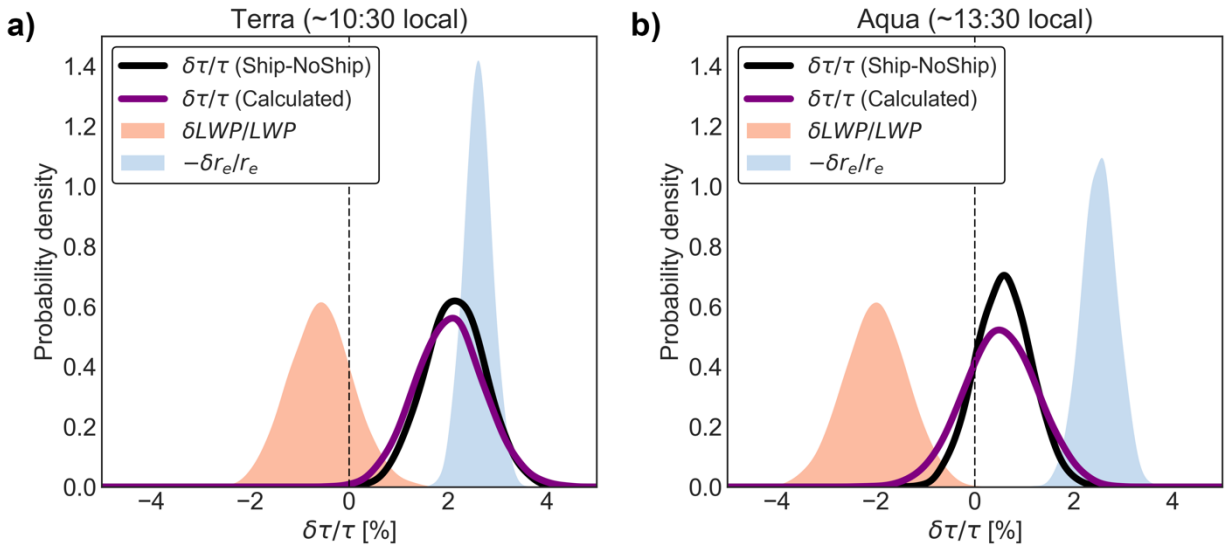

Figure 3. Cloud optical thickness changes from shipping in the subtropical southeast Atlantic. Decomposition of the relative cloud optical thickness changes (curves) into components related to changing liquid water path (red shading) and effective radius (blue shading) for **a)** MODIS/Terra and **b)** MODIS/Aqua. The Ship-NoShip estimate for the cloud optical thickness change is shown in black and the estimate calculated from the liquid water path and effective radius changes in purple. Probability densities are calculated from the 5,000 Ship-NoShip estimates for each variable via Gaussian KDE.

Although the increase in cloud optical thickness is dominated by the decrease in r_e in the morning, by afternoon, the decrease in liquid water path is sufficiently large to offset this effect. At least in this region, cloud adjustments partially counteract rather than enhance the Twomey effect.

5 Radiative impact

The estimated change in daily-average total albedo, or reflectivity, for the subtropical region, given the mean austral spring clear-sky downwelling shortwave radiation at the surface ($SW_{\downarrow}$), leads to an effective radiative forcing of -1.2 W/m^2 (95% confidence interval: -1.8 to -0.5 W/m^2) in the shipping corridor (Figure 4). (The negative sign of the radiative forcing means more shortwave energy is now leaving the Earth system.) The absolute value of this radiative forcing is two orders of magnitude greater than previous estimates for the southeast Atlantic region obtained from clearly visible ship tracks alone (Schreier et al., 2007).

The total albedo changes can be broken down into components due to changing cloud fraction and those due to changing cloud brightness as $\delta A \approx F_{cld}\delta A_{cld} + (A_{cld}-A_{clr})\delta F_{cld}$, where

A_{cld} is the cloud albedo and A_{clr} is the clear-sky albedo. We find that changes in cloud albedo alone explain virtually all of the observed change in total albedo. The radiative forcing from cloud fraction changes alone is small compared to that from changing cloud albedo and is not distinguishable from zero at the 95% confidence level. Hence, it follows that changes in cloud brightness, not fractional coverage, drive the all-sky albedo response to shipping in this region.

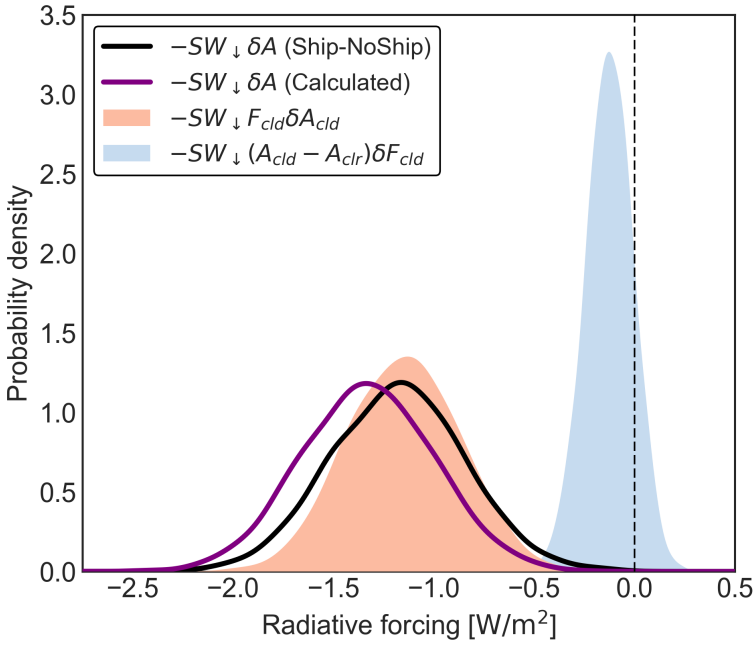

Figure 4. Radiative forcing from shipping-induced cloud changes in the subtropical southeast Atlantic. Decomposition of the total albedo change (curves) into components related to changing cloud albedo (red shading) and cloud fraction (blue shading) in the core of the shipping corridor. The Ship-NoShip estimate for the total albedo change is shown in black and the estimate calculated from cloud albedo and fractional coverage changes in purple. Albedo changes are multiplied by the mean austral spring insolation to produce radiative forcings. Probability densities are calculated from the 5,000 Ship-NoShip estimates for each variable via Gaussian KDE.

The Twomey effect (cloud brightening from increasing N_d alone) can be approximated as $\delta A_{cld,Twomey} \approx A_{cld}(1-A_{cld})/3\ \delta N_d/N_d$ (Platnick & Twomey, 1994). Figure 5 shows the cloud brightening that would be estimated from the change in N_d alone compared to the Ship-NoShip cloud albedo change estimates for the Terra and Aqua overpass times. In the morning, cloud brightening from the Twomey effect is consistent with the change in cloud albedo directly estimated from the Ship-NoShip differences, whereas during the afternoon, there is an offset. This is consistent with the decrease in liquid water path in the afternoon counteracting some of the brightening from increasing the cloud droplet number concentration.

The central estimate of the cloud albedo increase in the tropical region is also consistent with a dominant Twomey effect. However, because the cloud albedo change is neither field

significant nor statistically distinguishable from zero at the 95% confidence level, we refrain from drawing strong conclusions about cloud brightening in the tropical region.

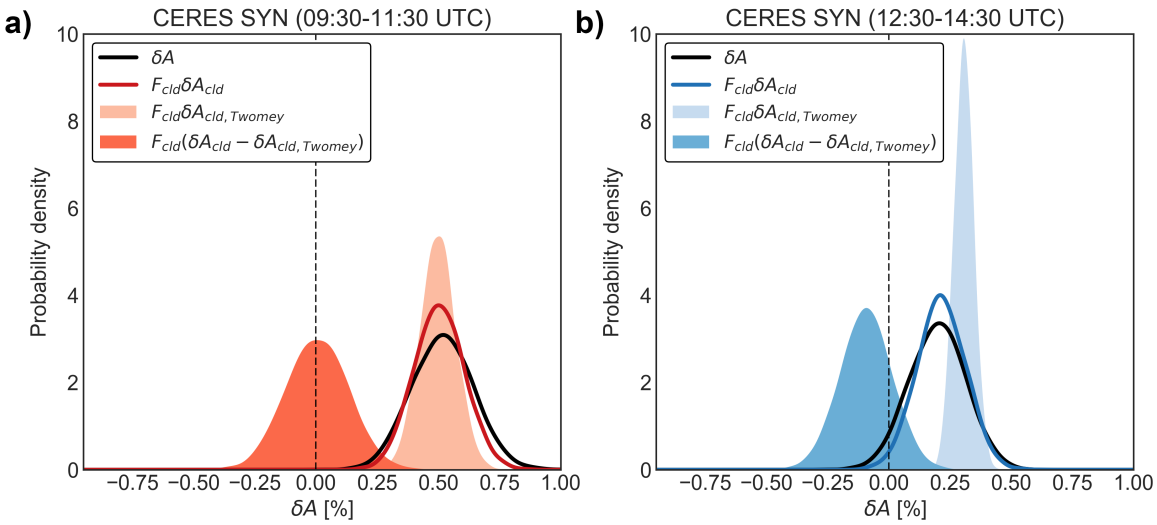

Figure 5. Estimated cloud brightening from the Twomey effect in the morning and afternoon. **a)** Ship-NoShip change in total albedo (black curve), total albedo change attributable to changes in cloud albedo (colored curve), total albedo change attributable to the Twomey effect alone (light shading), and the difference between the total albedo changes as calculated from the Ship-NoShip cloud albedo change and the Twomey effect estimate (dark shading) for the Terra overpass time period. **b)** as in a), but for the Aqua overpass time. Probability densities are calculated from the 5,000 Ship-NoShip estimates for each variable via Gaussian KDE.

6 The issue of detectability

6.1 Timescales of detectability

Here, we were able to demonstrate for the first time that climatically-relevant changes in cloud radiative forcing are generated by commercial shipping on regional spatial scales. However, we were only able to detect a robust response in the stratocumulus-dominated subtropical domain, not in the tropical domain where cumuliform clouds are more common. We argue that this may be a signal-to-noise question. In regions where the sensitivity of cloud properties and organization to meteorological variability is larger, such as the more tropical domain (George & Wood, 2010; Peters et al., 2014), longer time-series may be needed to average out the variability and to obtain the signal. Previous attempts to detect shipping perturbation were based on merely a few years of data, which may not have been sufficient to smooth out the noise. To test this hypothesis, we reprocess our results for N_d and A_{cld} in the subtropical domain using all combinations of individual years (e.g., austral spring of 2006

alone), consecutive two-year periods (e.g., austral spring in 2005 and 2006 only), consecutive three-year periods (e.g., austral spring 2005-2007 only), etc.

With only one or two years of data, it is possible to surmise the sign of the N_d effect but not its magnitude (Figure 6). Neither are necessarily clear for the A_{cld} effect. The estimates better approximate their climatological distributions once five to six years of data are available.

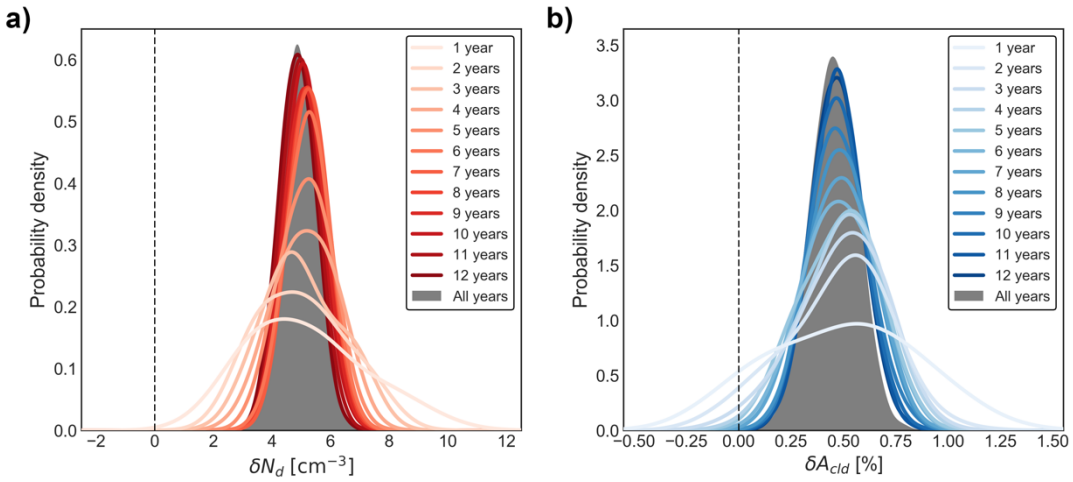

Figure 6. Probability distributions of temporally-subsampled results. **a)** Probability densities for the different consecutive-year averages (colored curves) and the 2003-2015 climatology (grey shading) for the MODIS/Aqua cloud droplet number concentration effect mean Ship-NoShip difference in the subtropical region. **b)** as in a), but for cloud albedo. Probability densities are estimated via Gaussian KDE for the 65,000 estimates of effect size in the thirteen single-year cases, 60,000 estimates of effect size in the twelve consecutive two-year cases, and so on, until we are left with the original 5,000 estimates for the full 13-year climatology.

Given the amount of time needed to detect clear signals for the relatively uniform stratocumulus clouds in the subtropical domain, the hypothesis that tropical clouds require a substantially longer record to be able to detect a signal above the noise seems plausible. As a further complication, remotely-sensed cloud properties are more uncertain in the tropical region due to the lower frequency of occurrence of clouds, three-dimensional radiative effects, heterogeneity of the cloud field, cloud-edge effects, and other biases (Bennartz & Rausch, 2017; Grosvenor et al., 2018).

It is also, of course, possible that the lack of detection of a strong shipping signal is not a result of observational limitations but rather a reflection that shipping effects truly are smaller in the tropical region. For instance, the marine boundary layer is deeper and more likely to be decoupled in this region, so the aerosols and precursor gases emitted by ships near the surface may not be efficiently transported to the subcloud layer. Additionally, it is possible that cumuliform clouds are less susceptible to aerosol-driven increased in N_d than stratiform clouds

due to differences in supersaturation adjustments between the two regimes (Jia, Ma, Yu, Liu, & Yin, 2019).

6.2 Implications for 2020 International Maritime Organization regulations

Our findings are undergoing a real-world test as International Maritime Organization regulations (International Maritime Organization, 2016; Sofiev et al., 2018) limiting fuel sulfur content to 0.5% by mass (from the present standard of 3.5%) come into effect as of January 1st, 2020. Although the fuel used will still contain some sulfur content, the particles produced by ships under the new regulations may be too small to effectively serve as cloud condensation nuclei at the relatively low supersaturations characteristic of marine stratocumulus clouds (Petzold et al., 2010). An analysis of the effect of reducing fuel-sulfur content restrictions from 1.0% to 0.1% in 2015 within the emission control area off the western coast of North America found a dramatic decrease in manually-detected ship tracks immediately following the strengthening of the regulation (Gryspeerdt, Smith, et al., 2019). The 2020 global IMO regulations are therefore likely to dramatically reduce the cooling effect of aerosol-cloud interactions associated with the global shipping industry. If our analysis is valid, we should be able to observe decreases in N_d and cloud albedo by the mid-2020s assuming the regulation is implemented fully and on-time.

6.3 Implications for marine cloud brightening

There are also practical implications of our detectability findings for the study of aerosol-cloud interactions generally, and in particular for possible field tests of marine cloud brightening (Latham et al., 2012; Wood et al., 2017; Wood & Ackerman, 2013). The first paper documenting ship tracks in the 1960s remarked that it may be possible to cool the climate via cloud-seeding over the oceans (Conover, 1966). More recently, interest has grown in exploring the feasibility of doing so to counteract anthropogenic warming due to greenhouse gas emissions (Latham, 1990; Latham et al., 2012; Lawrence et al., 2018). It has even been proposed that the international shipping fleet could alter the fuel it burns from low-sulfur near the coasts to higher-sulfur further offshore to capture some of the health benefits of reduced air pollution while maintaining most of the ships' cooling effects (Partanen et al., 2013).

The results here suggest that a regional-scale field test of marine cloud brightening in stratocumulus-dominated regions would likely be successful in terms of increasing cloud albedo; however, it may require several years for the regional perturbation to the outgoing shortwave energy flux to be clearly detectable via satellite remote sensing. This agrees well with previous work suggesting that multiple years of observations may be required to detect deliberate albedo modifications depending on the size and abruptness of the perturbation (Seidel, Feingold, Jacobson, & Loeb, 2014). If detection from space is considered a key criterion of success for the field test, this relatively large time commitment raises the question of at what point a regional

field test blurs into regional implementation of marine cloud brightening (Robock, Bunzl, Kravitz, & Stenchikov, 2010).

7 Observationally-informed global radiative forcing estimates

If we assume that that relationships between sulfate, cloud droplet number concentration, and cloud albedo calculated within the shipping corridor in the southeast Atlantic hold globally, we can estimate the present-day effective aerosol-cloud radiative forcing for a given increase in sulfate from pre-industrial times. The global estimate is obtained by combining estimates for cumuliform-type clouds from the tropical domain of the shipping corridor and estimates for stratiform-type clouds from the subtropical domain of the shipping corridor. Previous work has shown that the relationship between cloud droplet number concentration and MBL sulfate mass is similar across different stratocumulus-dominated ocean and land regions (McCoy et al., 2017). This suggests that our assumption that values derived in one particular region can represent similar cloud types across the globe is reasonable.

The mean ratio of present-day to pre-industrial surface sulfate mass concentrations from the CMIP6 models is shown in Figure 7a. The multi-model mean is calculated by first calculating the mean of all ensemble members of each model and then averaging all single-model means.

We calculate ERF_{ACI} by converting the ratio of present-day to pre-industrial sulfate ($SO_{4,PD}/SO_{4,PI}$) at each grid box into an estimate of increased cloud albedo. To do this, we define a relative albedo susceptibility (RAS) as $\delta\ln(A_{cld})/\delta\ln(SO_4)$ and use the tropical and subtropical CERES EBAF cloud albedo and MERRA-2 sulfate changes to calculate a value of 0.027 (95% confidence interval: -0.019 to 0.073) for cumuliform clouds and 0.053 (0.003 to 0.079) for stratiform clouds within the shipping corridor.

The ratio of present-day to pre-industrial cloud albedo can then be calculated by raising the sulfate ratio to the power of the relative albedo susceptibility: $A_{cld,PD}/A_{cld,PI} = (SO_{4,PD}/SO_{4,PI})^{RAS}$. (Note that the change in sulfate is large compared to the pre-industrial sulfate concentration whereas the change in cloud albedo is generally much smaller than the pre-industrial cloud albedo.) To get the absolute change in cloud albedo between the present-day and pre-industrial times, ΔA_{cld}, we must assume a value for the pre-industrial cloud albedo: $\Delta A_{cld} \equiv A_{cld,PI}\,(A_{cld,PD}/A_{cld,PI} - 1)$. We set the pre-industrial cloud albedo equal to the observed mean CERES EBAF cloud albedo for each of our regions/cloud regimes. The error from using the present-day value rather than the (unmeasurable) pre-industrial value is expected to be small compared to the other uncertainties accounted for in the analysis, as the $A_{cld,PD}/A_{cld,PI}$ values are generally close to unity (i.e., $RAS \ll 1$) across the globe and are lower than average in the Southern Hemisphere because of the regional sulfate distribution.

Because the EECRA stratiform and cumuliform cloud fractions are created using observations of clouds made from the surface, we must account for the masking of low cloud albedo changes by higher clouds before we can calculate the top-of-atmosphere ERF_{ACI}. We define “higher clouds” to be those with cloud top pressure values of less than 680 hPa and

calculate a higher cloud fraction, $F_{cld,<680}$, using the joint histograms of daytime cloud fraction and cloud top pressure from the standard MODIS product (values for Aqua and Terra are averaged to create a daytime average). We assume random overlap between high and low clouds.

Putting all of the above together, we calculate ERF_{ACI} for each grid box as:

$$ERF_{ACI} = -SW_{\downarrow} (1-F_{cld,<680}) F_{Sc/Cu} \Delta A_{cld},$$

where the clear-sky downwelling shortwave flux at the surface ($SW_{\downarrow}$) is now representative of the annual mean. ERF_{ACI} values are calculated separately for stratiform and cumuliform clouds using the cloud fraction and albedo change associated with each cloud type. The ERF_{ACI} for all low clouds is taken as the sum of the stratiform and cumuliform contributions. It should be noted that our estimates do not include potential cloud fraction adjustments, as we did not find any evidence for systematic cloud fraction changes in response to the shipping perturbation.

To generate a distribution of ERF_{ACI} values, for each of the 5,000 estimates of RAS, a model is chosen at random and then one ensemble member is chosen at random to provide the sulfate ratio that is then used to calculate the change in cloud albedo. The range of plausible ERF_{ACI} values thus accounts for both uncertainty in the kriging model as well as uncertainty due to the inter-model spread in sulfate increases.

Figure 7b-d provides global maps of the resulting mean ERF_{ACI} estimates for all low clouds, stratiform low clouds only, and cumuliform low clouds only. Unsurprisingly, ERF_{ACI} is greatest in the Northern Hemisphere, with particularly large values over Asia, North America, and the northeast Pacific Ocean. Despite having below-average increases in sulfate, the southeast Pacific and southeast Atlantic stratocumulus regions also have large ERF_{ACI} values due to their extensive coverage of low clouds (and relative lack of high clouds).

Global average ERF_{ACI} values are reported in Table 3 for each cloud type and their combination. In addition to the global averages, Table 3 also records global average values for the analysis performed over the oceans and land separately. The ERF_{ACI} from stratiform clouds is approximately twice as large as that from cumuliform clouds; however, the uncertainty in the total ERF_{ACI} from low clouds is dominated by the cumuliform cloud contribution. This is primarily due to the poor constraint from our CERES EBAF results in the tropical domain as compared to those found in the subtropical domain. The ERF_{ACI} from marine clouds is approximately twice as large as that from clouds over land.

Our global mean estimate of ERF_{ACI} in low clouds of -0.62 W/m^2 (95% confidence interval: -1.23 to -0.08 W/m^2) is very similar to the ERF_{ACI} estimate of -0.59 W/m^2 (2σ range of -1.21 to -0.03 W/m^2) derived from an analysis of climate model runs from Phase 5 of CMIP (CMIP5) that only included anthropogenic sulfate emissions (Zelinka, Andrews, Forster, & Taylor, 2014). Including all aerosol sources increases the ERF_{ACI} in Zelinka et al. (2014) to -0.92 W/m^2 (2σ range of -1.60 to -0.24 W/m^2). The most comparable value in the Fifth Assessment Report of the Intergovernmental Panel on Climate Change (Boucher et al., 2013; Myhre et al., 2013), -0.45 W/m^2 (90% confidence interval of -1.2 to 0.0 W/m^2), is lower than our central estimate but overall consistent within the considerable uncertainty. Our value is also well within the ERF_{ACI} range of -3.1 to -0.1 W/m^2 (95% confidence interval) from the global aerosol

radiative forcing review resulting from the 2018 World Climate Research Programme's Grand Science Challenge on Clouds, Circulation and Climate Sensitivity workshop at Schloss Ringberg (Bellouin et al., 2019). Assuming moderate values for the effective radiative forcing from aerosl-radiation interactions, our value can also accommodate the lower bound of total effective radiative forcing due to aerosol-radiation and aerosol-cloud interactions of -1.0 W/m^2 inferred from the historical record of warming between 1850-1950 in the Northern Hemisphere (Stevens, 2015). It should be noted that our estimate does not attempt to account for the different effects of aerosol-cloud interactions in mixed-phase and ice clouds, which are quite uncertain as well (Boucher et al., 2013; Possner, Ekman, & Lohmann, 2017).

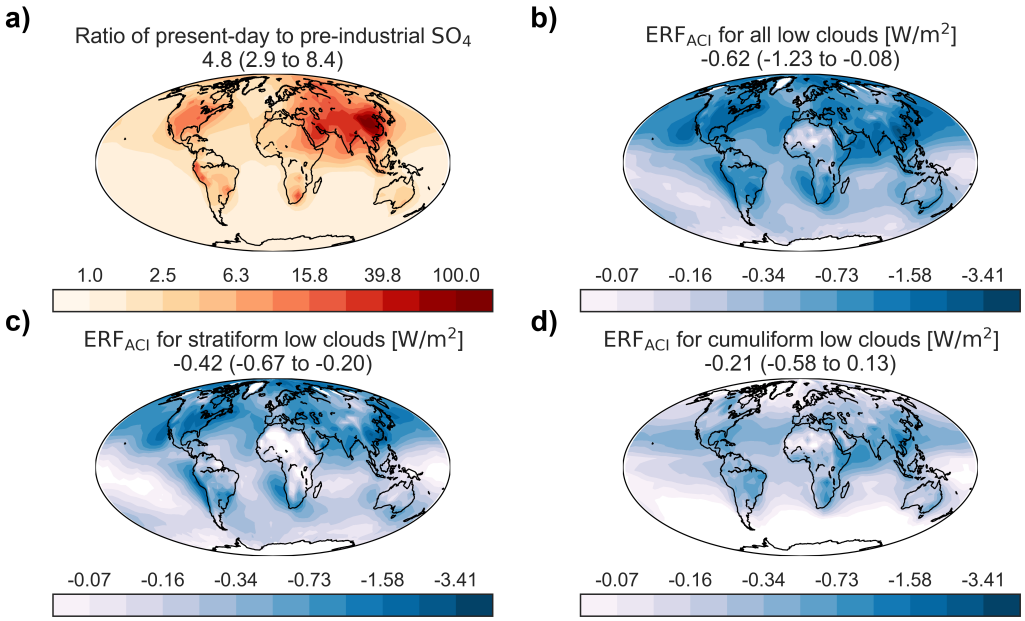

Figure 7. CMIP6 increases in sulfate burden and resulting effective radiative forcing due to aerosol-cloud interactions. Global maps of **a)** multi-model mean ratio of present-day to pre-industrial near-surface sulfate mass concentration and calculated ERF_{ACI} estimates for **b)** all low clouds, **c)** stratiform low clouds only, and **d)** cumuliform low clouds only. For each panel, globally-averaged mean values and 95% confidence intervals are provided below the title.

We can also use our results from shipping in the southeast Atlantic to provide an observationally-informed estimate of the radiative forcing from the Twomey effect alone through an analysis similar to that presented above and that can be found in McCoy et al. (2017). Relative cloud droplet number changes between the present-day and pre-industrial era, $\Delta\ln(N_d)$, are estimated using ACI parameters calculated using effective radius for MODIS/Terra and cloud droplet number concentration for MODIS/Aqua for each region as: $\Delta\ln(N_d) = (SO_{4,PD}/SO_{4,PI})^{ACI} - 1$. We then calculate the albedo increase due to the Twomey effect, $\Delta A_{cld,Twomey}$, as $\Delta A_{cld,Twomey} = A_{cld}(1-A_{cld})/3\ \Delta\ln(N_d)$ for Terra and Aqua separately and average the values together to create a daily-mean estimate for each region/cloud type. We set the cloud albedo as the relevant CERES SYN observed mean value; the factor $A_{cld}(1-A_{cld})/3$ is relatively insensitive to small changes in the value of cloud albedo, so the error associated with using the present-day rather

than the (unmeasurable) pre-industrial value is expected to be small. We then calculate the radiative forcing due to the Twomey effect as:

$RF_{Twomey} = -SW_{\downarrow} (1-F_{cld,<680}) F_{Sc/Cu} \Delta A_{cld,Twomey}$.

As with ERF_{ACI}, results for the globally averaged RF_{Twomey} values for each cloud type and their combination are reported in Table 3, along with ocean-only and land-only estimates. Our global mean RF_{Twomey} estimate of -0.69 W/m^2 (-0.98 to -0.45 W/m^2) is approximately one-third lower than the -0.97 W/m^2 estimate (full range of -1.3 to -0.61 W/m^2) from McCoy et al. (2017). The RF_{Twomey} values we calculate are ~10-20% higher than ERF_{ACI} for stratiform and all low clouds. This reflects our findings that cloud adjustments to the Twomey effect appear to be countervailing on net, at least during the day for stratiform clouds. Our overall uncertainty for the RF_{Twomey} estimates is lower than for ERF_{ACI} in large part because of the better constraints on MODIS cloud effective radius and cloud droplet number concentration changes as compared to changes in CERES cloud albedo in the tropical region.

Table 3. Estimates of radiative forcing (Twomey effect only) and effective radiative forcing (Twomey effect with cloud adjustments) due to aerosol-cloud interactions for stratiform, cumuliform, and all low clouds averaged globally, only over the oceans, and only over land.

	Stratiform low clouds	Cumuliform low clouds	All low clouds
Global ERF_{ACI} [W/m^2]	-0.42 (-0.67 to -0.20)	-0.21 (-0.58 to 0.13)	-0.62 (-1.23 to -0.08)
Global RF_{Twomey} [W/m^2]	-0.53 (-0.72 to -0.37)	-0.16 (-0.27 to -0.07)	-0.69 (-0.98 to -0.45)
Oceans-only ERF_{ACI} [W/m^2]	-0.28 (-0.48 to -0.13)	-0.12 (-0.35 to 0.08)	-0.41 (-0.81 to -0.07)
Oceans-only RF_{Twomey} [W/m^2]	-0.34 (-0.50 to -0.23)	-0.10 (-0.16 to -0.04)	-0.43 (-0.65 to -0.28)
Land-only ERF_{ACI} [W/m^2]	-0.13 (-0.21 to -0.06)	-0.08 (-0.23 to 0.05)	-0.21 (-0.44 to -0.01)
Land-only RF_{Twomey} [W/m^2]	-0.18 (-0.28 to -0.12)	-0.06 (-0.12 to -0.03)	-0.25 (-0.39 to -0.15)

8 Conclusions and future directions

We find the first observational evidence for substantial cloud microphysical and radiative impacts from shipping by using universal kriging to estimate cloud properties under the counterfactual situation of no shipping effects in the southeast Atlantic basin. All-sky albedo changes in the stratocumulus region are dominated by changes in cloud albedo, not in fractional cloudiness. This cloud brightening is driven by increases in droplet number and decreases in droplet size and is partially offset by decreases in liquid water path (at least in the afternoon).

Our results join a growing literature of studies using "natural experiments" like volcanic eruptions and the inadvertent modification of clouds from international shipping, which overall have tended to find that model estimates of the effective radiative forcing due to aerosol-cloud interactions are likely too negative due to overly strong adjustments that reinforce the Twomey effect (Gryspeerdt, Goren, et al., 2019; Malavelle et al., 2017; Toll et al., 2017; Toll et al., 2019). These previous papers, however, have taken a "bottom-up" approach of aggregating statistics of individual pollution tracks to reach their conclusions, whereas we take a "top-down" approach to study aerosol-cloud interactions using climatological fields. As automated methods of identifying individual ship tracks improve (Yuan et al., 2019) and other advances are made in

tracking airmasses affected by individual ships (Gryspeerdt, Smith, et al., 2019), these "bottom-up" and "top-down" methods should be able to converge and provide increased certainty about the net effect of cloud adjustments to aerosol perturbations.

Although the results from the "natural experiments" studies have tended to find small or countervailing cloud adjustments to the Twomey effect, other recent work attempting to control for aerosol-meteorology correlations by stratifying observations by cloud geometrical thickness has come to the opposite conclusion: That cloud adjustments to the Twomey effect are strong and tend to reinforce cooling, so much so that compensating warming effects of aerosols on deep convection must be invoked to maintain a realistic global energy balance (Rosenfeld et al., 2019). Based on the relative susceptibilities of cloud fraction and liquid water path from Table 1 of Rosenfeld et al. (2019), we would have expected a cloud fraction increase of 1.66% (0.89 to 2.55%) and a liquid water path increase of 0.15% (-0.70 to 1.00%) for the increase in cloud droplet number concentration from MODIS/Aqua in the subtropical region. (95% confidence intervals are calculated by multiplying the 5,000 Ship-NoShip relative N_d change estimates by random draws from a normal distribution with the mean and standard deviation of the susceptibility values.) Both of the estimates based on Rosenfeld et al. (2019) lie outside the 95% confidence intervals of the daytime cloud fraction and liquid water path estimates we found. If the true cloud fraction response in the subtropical southeast Atlantic were as large as suggested by the Rosenfeld et al. (2019) analysis, it seems unlikely that our method would not have been able to detect it. Whether other regions/seasons with lower baseline cloud fractions respond in the same manner as those in the southeast Atlantic in austral spring remains an open question, however. Overall, the "natural experiment" literature has thus far provided less insight into changes in fractional cloudiness than in liquid water path — a more dedicated analysis of cloud fraction changes in response to perturbations like shipping and volcanoes could be a promising avenue for future work.

Extrapolating our results globally, we calculate an effective radiative forcing due to aerosol-cloud interactions in low clouds of -0.62 W/m^2 (-1.23 to -0.08 W/m^2) and a radiative forcing due to the Twomey effect alone of -0.69 W/m^2 (-0.98 to -0.45 W/m^2). Cloud adjustments that lead to decreasing liquid water path during the day reduce the ERF_{ACI} from stratiform-type clouds by ~20% compared to the radiative forcing from the Twomey effect alone. The uncertainty in our global estimates is dominated by cumuliform clouds even though the central estimates of the forcings are about twice as large for stratiform clouds. Given the plausibility of either strong increases (Albrecht, 1989) or decreases (Seifert et al., 2015) in liquid water path in these clouds, the apparent difficulty of discerning observational signals in these clouds (Grosvenor et al., 2018; Peters et al., 2014), and the general absence of clear pollution tracks within this regime (Toll et al., 2019), better understanding cumuliform cloud responses should be a priority for those interested in better constraining ERF_{ACI}.

The unique setup in the southeast Atlantic provides an opportunity to study climate-scale cloud and radiative responses to a fairly well-known aerosol perturbation in which the causal relationship between aerosol and cloud changes is clear. Cloud microphysical changes in response to shipping emissions and the resulting cloud adjustments in this region could provide valuable benchmarks that can be used to evaluate the representation of the Twomey effect and

cloud adjustments in regional and global climate models and in competing observational strategies.

Data availability

EDGAR emissions data are publicly available at https://data.europa.eu/doi/10.2904/JRC_DATASET_EDGAR and http://edgar.jrc.ec.europa.eu/overview.php?v=432. MERRA-2 data are publicly available from NASA's Goddard Earth Sciences Data and Information Services Center at https://disc.gsfc.nasa.gov/daac-bin/FTPSubset2.pl. Standard MODIS data are publicly available from NASA's Level-1 and Atmosphere Archive & Distribution System Distributed Active Archive Center at https://ladsweb.modaps.eosdis.nasa.gov/. MODIS N_d data are publicly available from the Vanderbilt University Institutional Repository at http://hdl.handle.net/1803/8374. CERES data are publicly available from NASA's Langley Research Center at https://ceres-tool.larc.nasa.gov/ord-tool/jsp/EBAF4Selection.jsp for the EBAF top-of-atmosphere products, https://ceres-tool.larc.nasa.gov/ord-tool/jsp/EBAFSFC4Selection.jsp for the EBAF surface irradiances product, and https://ceres-tool.larc.nasa.gov/ord-tool/jsp/SYN1degEd4Selection.jsp for the SYN products. CMIP6 data are made publicly available by the World Climate Research Programme and are hosted by the U.S. Department of Energy's Lawrence Livermore National Laboratory at https://esgf-node.llnl.gov/projects/cmip6/. EECRA data are publicly available from the Climatic Atlas of Clouds Over Land and Ocean at https://atmos.uw.edu/CloudMap/.

Acknowledgments

M.S.D. was supported by NASA Headquarters under the NASA Earth and Space Science Fellowship Program, grant NNX-80NSSC17K0404. H.M.D. was supported by the National Science Foundation Graduate Research Fellowship under grant DGE-1256082. Additional funding for this work was provided by NASA Earth Venture Suborbital-2 grant NNX-15AF98G. The authors thank Sarah Doherty, Roger Marchand, Samuel Pennypacker, Adrian Raftery, Daniel Rosenfeld, Michelle Shaffer, and Paquita Zuidema for helpful comments and suggestions. M.S.D. and H.M.D. thank the University of Washington's Program on Climate Change for providing a catalyst for interdisciplinary collaborations.

Author contribution

M.S.D., A.P., and R.W. conceived this study. M.S.D. and H.M.D. designed and implemented the methods. R.E. supplied the stratiform and cumuliform cloud fraction products. M.S.D. analyzed the results and all authors contributed to their interpretation. M.S.D. drafted the manuscript with the input of all coauthors.

References

Ackerman, A. S., Kirkpatrick, M. P., Stevens, D. E., & Toon, O. B. (2004). The impact of humidity above stratiform clouds on indirect aerosol climate forcing. *Nature, 432*, 1014. doi:10.1038/nature03174

Ackerman, A. S., Toon, O. B., Taylor, J. P., Johnson, D. W., Hobbs, P. V., & Ferek, R. J. (2000). Effects of Aerosols on Cloud Albedo: Evaluation of Twomey's Parameterization of Cloud Susceptibility Using Measurements of Ship Tracks. *Journal of the Atmospheric Sciences, 57*(16), 2684-2695. doi:10.1175/1520-0469(2000)057<2684:Eoaoca>2.0.Co;2

Adebiyi, A. A., Zuidema, P., & Abel, S. J. (2015). The Convolution of Dynamics and Moisture with the Presence of Shortwave Absorbing Aerosols over the Southeast Atlantic. *Journal of Climate, 28*(5), 1997-2024. doi:10.1175/jcli-d-14-00352.1

Albrecht, B. A. (1989). Aerosols, Cloud Microphysics, and Fractional Cloudiness. *Science, 245*, 1227-1230. doi:10.1126/science.245.4923.1227

Andreae, M. O., Jones, C. D., & Cox, P. M. (2005). Strong present-day aerosol cooling implies a hot future. *Nature, 435*(7046), 1187-1190. doi:10.1038/nature03671

Beijing Climate Center (2018). *BCC BCC-ESM1 model output prepared for CMIP6 CMIP historical*. Earth System Grid Federation. Version 20191011. http://cera-www.dkrz.de/WDCC/meta/CMIP6/CMIP6.CMIP.BCC.BCC-ESM1.historical

Bellouin, N., Quaas, J., Gryspeerdt, E., Kinne, S., Stier, P., Watson-Parris, D., . . . Stevens, B. (2019). Bounding global aerosol radiative forcing of climate change. *Reviews of Geophysics*. doi:10.1029/2019rg000660

Benjamini, Y., & Hochberg, Y. (1995). Controlling the False Discovery Rate: A Practical and Powerful Approach to Multiple Testing. *Journal of the Royal Statistical Society. Series B (Methodological), 57*(1), 289-300. Retrieved from http://www.jstor.org/stable/2346101

Bennartz, R., & Rausch, J. (2017). Global and regional estimates of warm cloud droplet number concentration based on 13 years of AQUA-MODIS observations. *Atmospheric Chemistry and Physics, 17*(16), 9815-9836. doi:10.5194/acp-17-9815-2017

Boucher, O., Randall, D., Artaxo, P., Bretherton, C., Feingold, G., Forster, P. M., . . . Zhang, X. Y. (2013). Clouds and Aerosols. In T.F. Stocker, D. Qin, G.-K. Plattner, M. Tignor, S.K. Allen, J. Doschung, A. Nauels, Y. Xia, V. Bex, & P. M. Midgley (Eds.), *Climate Change 2013: The Physical Science Basis. Contribution of Working Group I to the Fifth Assessment Report of the Intergovernmental Panel on Climate Change* (pp. 571-657): Cambridge University Press.

Breon, F. M., Tanre, D., & Generoso, S. (2002). Aerosol effect on cloud droplet size monitored from satellite. *Science, 295*(5556), 834-838. doi:10.1126/science.1066434

Bretherton, C. S., Blossey, P. N., & Uchida, J. (2007). Cloud droplet sedimentation, entrainment efficiency, and subtropical stratocumulus albedo. *Geophysical Research Letters, 34*(3). doi:10.1029/2006gl027648

Campmany, E., Grainger, R. G., Dean, S. M., & Sayer, A. M. (2009). Automatic detection of ship tracks in ATSR-2 satellite imagery. *Atmospheric Chemistry and Physics, 9*(6), 1899-1905. doi:10.5194/acp-9-1899-2009

Capaldo, K., Corbett, J. J., Kasibhatla, P., Fischbeck, P., & Pandis, S. N. (1999). Effects of ship emissions on sulphur cycling and radiative climate forcing over the ocean. *Nature, 400*, 743. doi:10.1038/23438

Chen, Y. C., Christensen, M. W., Xue, L., Sorooshian, A., Stephens, G. L., Rasmussen, R. M., & Seinfeld, J. H. (2012). Occurrence of lower cloud albedo in ship tracks. *Atmospheric Chemistry and Physics, 12*(17), 8223-8235. doi:10.5194/acp-12-8223-2012

Coakley, J. A., & Walsh, C. D. (2002). Limits to the Aerosol Indirect Radiative Effect Derived from Observations of Ship Tracks. *Journal of the Atmospheric Sciences, 59*(3), 668-680. doi:10.1175/1520-0469(2002)059<0668:Lttair>2.0.Co;2

Conover, J. H. (1966). Anomalous Cloud Lines. *Journal of the Atmospheric Sciences, 23*(6), 778-785. doi:10.1175/1520-0469(1966)023<0778:Acl>2.0.Co;2

Crippa, M., Guizzardi, D., Muntean, M., Schaaf, E., Dentener, F., van Aardenne, J. A., . . . Janssens-Maenhout, G. (2018). Gridded emissions of air pollutants for the period 1970–2012 within EDGAR v4.3.2. *Earth System Science Data, 10*(4), 1987-2013. doi:10.5194/essd-10-1987-2018

Danabasoglu, Gokhan (2019). *NCAR CESM2-WACCM model output prepared for CMIP6 CMIP historical*. Version 20191011. Earth System Grid Federation. https://doi.org/10.22033/ESGF/CMIP6.10071

Danabasoglu, Gokhan; Lawrence, David; Lindsay, Keith; Lipscomb, William; Strand, Gary (2019). *NCAR CESM2 model output prepared for CMIP6 CMIP historical*. Version 20191011. Earth System Grid Federation. https://doi.org/10.22033/ESGF/CMIP6.7627

Eastman, R., Warren, S. G., & Hahn, C. J. (2011). Variations in Cloud Cover and Cloud Types over the Ocean from Surface Observations, 1954–2008. *Journal of Climate, 24*(22), 5914-5934. doi:10.1175/2011jcli3972.1

Eyring, V., Isaksen, I. S. A., Berntsen, T., Collins, W. J., Corbett, J. J., Endresen, O., . . . Stevenson, D. S. (2010). Transport impacts on atmosphere and climate: Shipping. *Atmospheric Environment, 44*(37), 4735-4771. doi:10.1016/j.atmosenv.2009.04.059

Feingold, G., Remer, L. A., Ramaprasad, J., & Kaufman, Y. J. (2001). Analysis of smoke impact on clouds in Brazilian biomass burning regions: An extension of Twomey's approach. *Journal of Geophysical Research, 106*(D19), 22907-22922. doi:doi:10.1029/2001JD000732

Gelaro, R., McCarty, W., Suárez, M. J., Todling, R., Molod, A., Takacs, L., . . . Zhao, B. (2017). The Modern-Era Retrospective Analysis for Research and Applications, Version 2 (MERRA-2). *Journal of Climate, 30*(14), 5419-5454. doi:10.1175/jcli-d-16-0758.1

George, R. C., & Wood, R. (2010). Subseasonal variability of low cloud radiative properties over the southeast Pacific Ocean. *Atmospheric Chemistry and Physics, 10*(8), 4047-4063. doi:10.5194/acp-10-4047-2010

Grosvenor, D. P., Sourdeval, O., Zuidema, P., Ackerman, A., Alexandrov, M. D., Bennartz, R., . . . Quaas, J. (2018). Remote Sensing of Droplet Number Concentration in Warm Clouds: A Review of the Current State of Knowledge and Perspectives. *Reviews of Geophysics, 56*, 409–453. doi:10.1029/2017rg000593

Gryspeerdt, E., Goren, T., Sourdeval, O., Quaas, J., Mülmenstädt, J., Dipu, S., . . . Christensen, M. (2019). Constraining the aerosol influence on cloud liquid water path. *Atmospheric Chemistry and Physics, 19*(8), 5331-5347. doi:10.5194/acp-19-5331-2019

Gryspeerdt, E., Quaas, J., & Bellouin, N. (2016). Constraining the aerosol influence on cloud fraction. *Journal of Geophysical Research: Atmospheres, 121*(7), 3566-3583. doi:10.1002/2015jd023744

Gryspeerdt, E., Smith, T. W. P., O'Keeffe, E., Christensen, M. W., & Goldsworth, F. W. (2019). The Impact of Ship Emission Controls Recorded by Cloud Properties. *Geophysical Research Letters*. doi:10.1029/2019gl084700

Guo, Huan; John, Jasmin G; Blanton, Chris; McHugh, Colleen; Nikonov, Serguei; Radhakrishnan, Aparna; Zadeh, Niki T.; Balaji, V; Durachta, Jeff; Dupuis, Christopher; Menzel, Raymond; Robinson, Thomas; Underwood, Seth; Vahlenkamp, Hans; Dunne, Krista A.; Gauthier, Paul PG; Ginoux, Paul; Griffies, Stephen M.; Hallberg, Robert; Harrison, Matthew; Hurlin, William; Malyshev, Sergey; Naik, Vaishali; Paulot, Fabien; Paynter, David J; Ploshay, Jeffrey; Schwarzkopf, Daniel M; Seman, Charles J; Shao, Andrew; Silvers, Levi; Wyman, Bruce; Zeng, Yujin; Adcroft, Alistair; Dunne, John P.; Held, Isaac M; Krasting, John P.; Horowitz, Larry W.; Milly, P.C.D; Shevliakova, Elena; Winton, Michael; Zhao, Ming (2018). *NOAA-GFDL GFDL-CM4 model output prepared for CMIP6 CMIP historical*. Version 20191011. Earth System Grid Federation. https://doi.org/10.22033/ESGF/CMIP6.8594

Hajima, Tomohiro; Kawamiya, Michio (2019). *MIROC MIROC-ES2L model output prepared for CMIP6 CMIP historical*. Version 20191011. Earth System Grid Federation. https://doi.org/10.22033/ESGF/CMIP6.5602

Hobbs, P. V., Garrett, T. J., Ferek, R. J., Strader, S. R., Hegg, D. A., Frick, G. M., . . . Innis, G. (2000). Emissions from Ships with respect to Their Effects on Clouds. *Journal of the Atmospheric Sciences, 57*(16), 2570-2590. doi:10.1175/1520-0469(2000)057<2570:Efswrt>2.0.Co;2

Hubanks, P. A., Platnick, S., King, M. D., & Ridgway, W. (2019). MODIS Atmosphere L3 Gridded Product Algorithm Theoretical Basis Document (ATBD) & Users Guide. Retrieved from https://modis-atmosphere.gsfc.nasa.gov/sites/default/files/ModAtmo/L3_ATBD_C6_C61_2019_02_20.pdf

International Maritime Organization. (2016). *Resolution MEPC.280(70): Effective Date of Implementation of the Fuel Oil Standard in Regulation 14.1.3 of MARPOL Annex VI.* Retrieved from http://www.imo.org/en/KnowledgeCentre/IndexofIMOResolutions/Marine-Environment-Protection-Committee-(MEPC)/Documents/MEPC.280(70).pdf

Jia, H., Ma, X., Yu, F., Liu, Y., & Yin, Y. (2019). Distinct Impacts of Increased Aerosols on Cloud Droplet Number Concentration of Stratus/Stratocumulus and Cumulus. *Geophysical Research Letters*. doi:10.1029/2019gl085081

Kato, S., Rose, F. G., Rutan, D. A., Thorsen, T. J., Loeb, N. G., Doelling, D. R., . . . Ham, S.-H. (2018). Surface Irradiances of Edition 4.0 Clouds and the Earth's Radiant Energy System (CERES) Energy Balanced and Filled (EBAF) Data Product. *Journal of Climate, 31*(11), 4501-4527. doi:10.1175/jcli-d-17-0523.1

Klein, S. A., Hartmann, D. L., & Norris, J. R. (1995). On the Relationships among Low-Cloud Structure, Sea Surface Temperature, and Atmospheric Circulation in the Summertime Northeast Pacific. *Journal of Climate, 8*(5), 1140-1155. doi:10.1175/1520-0442(1995)008<1140:Otralc>2.0.Co;2

Krasting, John P.; John, Jasmin G; Blanton, Chris; McHugh, Colleen; Nikonov, Serguei; Radhakrishnan, Aparna; Rand, Kristopher; Zadeh, Niki T.; Balaji, V; Durachta, Jeff; Dupuis, Christopher; Menzel, Raymond;

Robinson, Thomas; Underwood, Seth; Vahlenkamp, Hans; Dunne, Krista A.; Gauthier, Paul PG; Ginoux, Paul; Griffies, Stephen M.; Hallberg, Robert; Harrison, Matthew; Hurlin, William; Malyshev, Sergey; Naik, Vaishali; Paulot, Fabien; Paynter, David J; Ploshay, Jeffrey; Schwarzkopf, Daniel M; Seman, Charles J; Silvers, Levi; Wyman, Bruce; Zeng, Yujin; Adcroft, Alistair; Dunne, John P.; Guo, Huan; Held, Isaac M; Horowitz, Larry W.; Milly, P.C.D; Shevliakova, Elena; Stock, Charles; Winton, Michael; Zhao, Ming (2018). *NOAA-GFDL GFDL-ESM4 model output prepared for CMIP6 CMIP historical*. Version 20191011. Earth System Grid Federation. https://doi.org/10.22033/ESGF/CMIP6.8597

Latham, J. (1990). Control of global warming? *Nature, 347*(6291), 339-340. doi:10.1038/347339b0

Latham, J., Bower, K., Choularton, T., Coe, H., Connolly, P., Cooper, G., . . . Wood, R. (2012). Marine cloud brightening. *Philosophical Transactions of the Royal Society A: Mathematical, Physical and Engineering Sciences, 370*(1974), 4217-4262. doi:doi:10.1098/rsta.2012.0086

Lauer, A., Eyring, V., Hendricks, J., Jöckel, P., & Lohmann, U. (2007). Global model simulations of the impact of ocean-going ships on aerosols, clouds, and the radiation budget. *Atmospheric Chemistry and Physics, 7*(19), 5061-5079. doi:10.5194/acp-7-5061-2007

Lawrence, M. G., Schafer, S., Muri, H., Scott, V., Oschlies, A., Vaughan, N. E., . . . Scheffran, J. (2018). Evaluating climate geoengineering proposals in the context of the Paris Agreement temperature goals. *Nat Commun, 9*(1), 3734. doi:10.1038/s41467-018-05938-3

Loeb, N. G., Doelling, D. R., Wang, H., Su, W., Nguyen, C., Corbett, J. G., . . . Kato, S. (2018). Clouds and the Earth's Radiant Energy System (CERES) Energy Balanced and Filled (EBAF) Top-of-Atmosphere (TOA) Edition-4.0 Data Product. *Journal of Climate, 31*(2), 895-918. doi:10.1175/jcli-d-17-0208.1

Malavelle, F. F., Haywood, J. M., Jones, A., Gettelman, A., Clarisse, L., Bauduin, S., . . . Thordarson, T. (2017). Strong constraints on aerosol-cloud interactions from volcanic eruptions. *Nature, 546*(7659), 485-491. doi:10.1038/nature22974

Martin, G. M., Johnson, D. W., & Spice, A. (1994). The Measurement and Parameterization of Effective Radius of Droplets in Warm Stratocumulus Clouds. *Journal of the Atmospheric Sciences, 51*(13), 1823-1842.

Mauger, G. S., & Norris, J. R. (2010). Assessing the Impact of Meteorological History on Subtropical Cloud Fraction. *Journal of Climate, 23*(11), 2926-2940. doi:10.1175/2010jcli3272.1

McComiskey, A., Feingold, G., Frisch, A. S., Turner, D. D., Miller, M. A., Chiu, J. C., . . . Ogren, J. A. (2009). An assessment of aerosol-cloud interactions in marine stratus clouds based on surface remote sensing. *Journal of Geophysical Research, 114*(D9). doi:10.1029/2008jd011006

McCoy, D. T., Bender, F. A.-M., Mohrmann, J. K. C., Hartmann, D. L., Wood, R., & Grosvenor, D. P. (2017). The global aerosol-cloud first indirect effect estimated using MODIS, MERRA, and AeroCom. *Journal of Geophysical Research: Atmospheres, 122*(3), 1779-1796. doi:10.1002/2016JD026141

McCoy, D. T., & Hartmann, D. L. (2015). Observations of a substantial cloud-aerosol indirect effect during the 2014–2015 Bárðarbunga-Veiðivötn fissure eruption in Iceland. *Geophysical Research Letters, 42*(23), 10,409-410,414. doi:10.1002/2015gl067070

Myhre, G., Shindell, D., Bréon, F.-M., Collins, W., Fuglestvedt, J., Huang, J., . . . Zhang, H. (2013). Anthropogenic and Natural Radiative Forcing. In T. F. Stocker, D. Qin, G.-K. Plattner, M. Tignor, S. K. Allen, J. Boschung, A. Nauels, Y. Xia, V. Bex, & P. M. Midgley (Eds.), *Climate Change 2013: The Physical Science Basis. Contribution of Working Group I to the Fifth Assessment Report of the Intergovernmental Panel on Climate Change*. Cambridge, United Kingdom and New York, NY, USA: Cambridge University Press.

NorESM Climate modeling Consortium (2018). *NCC NorESM2-LM model output prepared for CMIP6 CMIP historical*. Version 20191114. Earth System Grid Federation. http://cera-www.dkrz.de/WDCC/meta/CMIP6/CMIP6.CMIP.NCC.NorESM2-LM.historical

Oreopoulos, L., & Platnick, S. (2008). Radiative susceptibility of cloudy atmospheres to droplet number perturbations: 2. Global analysis from MODIS. *Journal of Geophysical Research, 113*(D14). doi:10.1029/2007jd009655

Partanen, A. I., Laakso, A., Schmidt, A., Kokkola, H., Kuokkanen, T., Pietikäinen, J. P., . . . Korhonen, H. (2013). Climate and air quality trade-offs in altering ship fuel sulfur content. *Atmospheric Chemistry and Physics, 13*(23), 12059-12071. doi:10.5194/acp-13-12059-2013

Peters, K., Quaas, J., & Graßl, H. (2011). A search for large-scale effects of ship emissions on clouds and radiation in satellite data. *Journal of Geophysical Research, 116*, D24205. doi:10.1029/2011jd016531

Peters, K., Quaas, J., Stier, P., & Graßl, H. (2014). Processes limiting the emergence of detectable aerosol indirect effects on tropical warm clouds in global aerosol-climate model and satellite data. *Tellus B: Chemical and Physical Meteorology, 66*(1). doi:10.3402/tellusb.v66.24054

Petzold, A., Weingartner, E., Hasselbach, J., Lauer, P., Kurok, C., & Fleischer, F. (2010). Physical Properties, Chemical Composition, and Cloud Forming Potential of Particulate Emissions from a Marine Diesel Engine at Various Load Conditions. *Environmental Science & Technology, 44*(10), 3800-3805. doi:10.1021/es903681z

Platnick, S., & Twomey, S. (1994). Determining the Susceptibility of Cloud Albedo to Changes in Droplet Concentration with the Advanced Very High Resolution Radiometer. *Journal of Applied Meteorology, 33*(3), 334-347. doi:10.1175/1520-0450(1994)033<0334:dtsoca>2.0.co;2

Possner, A., Ekman, A. M. L., & Lohmann, U. (2017). Cloud response and feedback processes in stratiform mixed-phase clouds perturbed by ship exhaust. *Geophysical Research Letters*. doi:10.1002/2016gl071358

Possner, A., Wang, H., Wood, R., Caldeira, K., & Ackerman, T. (2018). The efficacy of aerosol-cloud-radiative perturbations from near-surface emissions in deep open-cell stratocumuli. *Atmospheric Chemistry and Physics, 18*, 17475-17488. doi:10.5194/acp-18-17475-2018

R Core Team. (2019). R: A Language and Environment for Statistical Computing. Vienna, Austria: R Foundation for Statistical Computing. Retrieved from https://www.R-project.org/

Randles, C. A., Da Silva, A. M., Buchard, V., Colarco, P. R., Darmenov, A., Govindaraju, R., . . . Flynn, C. J. (2017). The MERRA-2 Aerosol Reanalysis, 1980 - onward, Part I: System Description and Data Assimilation Evaluation. *Journal of Climate, 30*(17), 6823-6850. doi:10.1175/JCLI-D-16-0609.1

Ribeiro, P. A., & Diggle, P. J. (2018). geoR: Analysis of Geostatistical Data. R package version 1.7-5.2.1. Retrieved from https://CRAN.R-project.org/package=geoR

Ridley, Jeff; Menary, Matthew; Kuhlbrodt, Till; Andrews, Martin; Andrews, Tim (2019). *MOHC HadGEM3-GC31-LL model output prepared for CMIP6 CMIP historical*. Version 20191011. Earth System Grid Federation. https://doi.org/10.22033/ESGF/CMIP6.6109

Righi, M., Klinger, C., Eyring, V., Hendricks, J., Lauer, A., & Petzold, A. (2011). Climate impact of biofuels in shipping: global model studies of the aerosol indirect effect. *Environmental Science & Technology, 45*(8), 3519-3525. doi:10.1021/es1036157

Robock, A., Bunzl, M., Kravitz, B., & Stenchikov, G. L. (2010). A Test for Geoengineering? *Science, 327*(5965), 530-531. doi:10.1126/science.1186237

Rosenfeld, D., Zhu, Y., Wang, M., Zheng, Y., Goren, T., & Yu, S. (2019). Aerosol-driven droplet concentrations dominate coverage and water of oceanic low level clouds. *Science, 363*, eaav0566. doi:10.1126/science.aav0566 %J Science

Sandu, I., Brenguier, J.-L., Geoffroy, O., Thouron, O., & Masson, V. (2008). Aerosol Impacts on the Diurnal Cycle of Marine Stratocumulus. *Journal of the Atmospheric Sciences, 65*(8), 2705-2718. doi:10.1175/2008jas2451.1

Schreier, M., Mannstein, H., Eyring, V., & Bovensmann, H. (2007). Global ship track distribution and radiative forcing from 1 year of AATSR data. *Geophysical Research Letters, 34*(17). doi:10.1029/2007gl030664

Seferian, Roland (2018). *CNRM-CERFACS CNRM-ESM2-1 model output prepared for CMIP6 CMIP historical*. Version 20191011. Earth System Grid Federation. https://doi.org/10.22033/ESGF/CMIP6.4068

Seidel, D. J., Feingold, G., Jacobson, A. R., & Loeb, N. (2014). Detection limits of albedo changes induced by climate engineering. *Nature Climate Change, 4*(2), 93-98. doi:10.1038/nclimate2076

Seifert, A., Heus, T., Pincus, R., & Stevens, B. (2015). Large-eddy simulation of the transient and near-equilibrium behavior of precipitating shallow convection. *Journal of Advances in Modeling Earth Systems, 7*(4), 1918-1937. doi:10.1002/2015ms000489

Sofiev, M., Winebrake, J. J., Johansson, L., Carr, E. W., Prank, M., Soares, J., . . . Corbett, J. J. (2018). Cleaner fuels for ships provide public health benefits with climate tradeoffs. *Nat Commun, 9*(1), 406. doi:10.1038/s41467-017-02774-9

Stevens, B. (2015). Rethinking the Lower Bound on Aerosol Radiative Forcing. *Journal of Climate, 28*(12), 4794-4819. doi:10.1175/jcli-d-14-00656.1

Stevens, B., & Feingold, G. (2009). Untangling aerosol effects on clouds and precipitation in a buffered system. *Nature, 461*(7264), 607-613. doi:10.1038/nature08281

Toll, V., Christensen, M., Gassó, S., & Bellouin, N. (2017). Volcano and Ship Tracks Indicate Excessive Aerosol-Induced Cloud Water Increases in a Climate Model. *Geophysical Research Letters*. doi:10.1002/2017gl075280

Toll, V., Christensen, M., Quaas, J., & Bellouin, N. (2019). Weak average liquid-cloud-water response to anthropogenic aerosols. *Nature, 572*(7767), 51-55. doi:10.1038/s41586-019-1423-9

Twomey, S. (1974). Pollution and the Planetary Albedo. *Atmospheric Environment, 8*, 1251-1256.

Twomey, S. (1977). The Influence of Pollution on the Shortwave Albedo of Clouds. *Journal of the Atmospheric Sciences, 34*(7), 1149-1152. doi:10.1175/1520-0469(1977)034<1149:tiopot>2.0.co;2

Volodin, Evgeny; Mortikov, Evgeny; Gritsun, Andrey; Lykossov, Vasily; Galin, Vener; Diansky, Nikolay; Gusev, Anatoly; Kostrykin, Sergey; Iakovlev, Nikolay; Shestakova, Anna; Emelina, Svetlana (2019a). *INM INM-CM4-8 model output prepared for CMIP6 CMIP historical*. Version 20191114. Earth System Grid Federation. https://doi.org/10.22033/ESGF/CMIP6.5069

Volodin, Evgeny; Mortikov, Evgeny; Gritsun, Andrey; Lykossov, Vasily; Galin, Vener; Diansky, Nikolay; Gusev, Anatoly; Kostrykin, Sergey; Iakovlev, Nikolay; Shestakova, Anna; Emelina, Svetlana (2019b). *INM INM-CM5-0 model output prepared for CMIP6 CMIP historical*. Version 20191114. Earth System Grid Federation. https://doi.org/10.22033/ESGF/CMIP6.5070

Warren, S. G., Hahn, C. H., London, J., Chervin, R. M., & Jenne, R. L. (1986). Global Distribution of Total Cloud Cover and Cloud Type Amounts over Land. *University Corporation for Atmospheric Research, NCAR Technical Note TN-273+STR*. doi:doi:10.5065/D6GH9FXB

Warren, S. G., Hahn, C. H., London, J., Chervin, R. M., & Jenne, R. L. (1988). Global Distribution of Total Cloud Cover and Cloud Type Amounts Over the Ocean. *University Corporation for Atmospheric Research, NCAR Technical Note TN-317+STR*. doi:doi:10.5065/D6QC01D1

Wood, R. (2007). Cancellation of Aerosol Indirect Effects in Marine Stratocumulus through Cloud Thinning. *Journal of the Atmospheric Sciences, 64*(7), 2657-2669. doi:10.1175/jas3942.1

Wood, R., Ackerman, T., Rasch, P., & Wanser, K. (2017). Could geoengineering research help answer one of the biggest questions in climate science? *Earth's Future*. doi:10.1002/2017ef000601

Wood, R., & Ackerman, T. P. (2013). Defining success and limits of field experiments to test geoengineering by marine cloud brightening. *Climatic Change, 121*(3), 459-472. doi:10.1007/s10584-013-0932-z

Yuan, T., Wang, C., Song, H., Platnick, S., Meyer, K., & Oreopoulos, L. (2019). Automatically Finding Ship Tracks to Enable Large-Scale Analysis of Aerosol-Cloud Interactions. *Geophysical Research Letters, 46*(13), 7726-7733. doi:10.1029/2019gl083441

Zelinka, M. D., Andrews, T., Forster, P. M., & Taylor, K. E. (2014). Quantifying components of aerosol-cloud-radiation interactions in climate models. *Journal of Geophysical Research: Atmospheres, 119*(12), 7599-7615. doi:10.1002/2014jd021710

Zimmerman, D. L., & Stein, M. (2010). Classical Geostatistical Methods. In A. E. Gelfand, P. J. Diggle, M. Fuentes, & P. Guttorp (Eds.), *Handbook of Spatial Statistics* (pp. 29-44).

AGU Advances

Supporting Information for

Substantial Cloud Brightening from Shipping in Subtropical Low Clouds

Michael S. Diamond[1,2], Hannah M. Director[3,2], Ryan Eastman[1], Anna Possner[4], Robert Wood[1]

[1]Department of Atmospheric Sciences, University of Washington, Seattle, USA.

[2]Program on Climate Change, University of Washington, Seattle, USA.

[3]Department of Statistics, University of Washington, Seattle, USA.

[4]Institute for Atmosphere and Environmental Sciences, Goethe University in Frankfurt, Germany.

Contents of this file

Introduction

This file contains supporting information documenting the binned empirical variograms and fitted variograms used to estimate the stationary error term in the universal kriging model for the subtropical and tropical regions (Figures S1 and S2, respectively); the CMIP6 models used to estimate global radiative forcing (Table S1); and the regressors used, transformations applied (if any), and total number of individually significant grid boxes (out of 40 possible) for each variable analyzed in the subtropical and tropical regions (Tables S2 and S3, respectively).

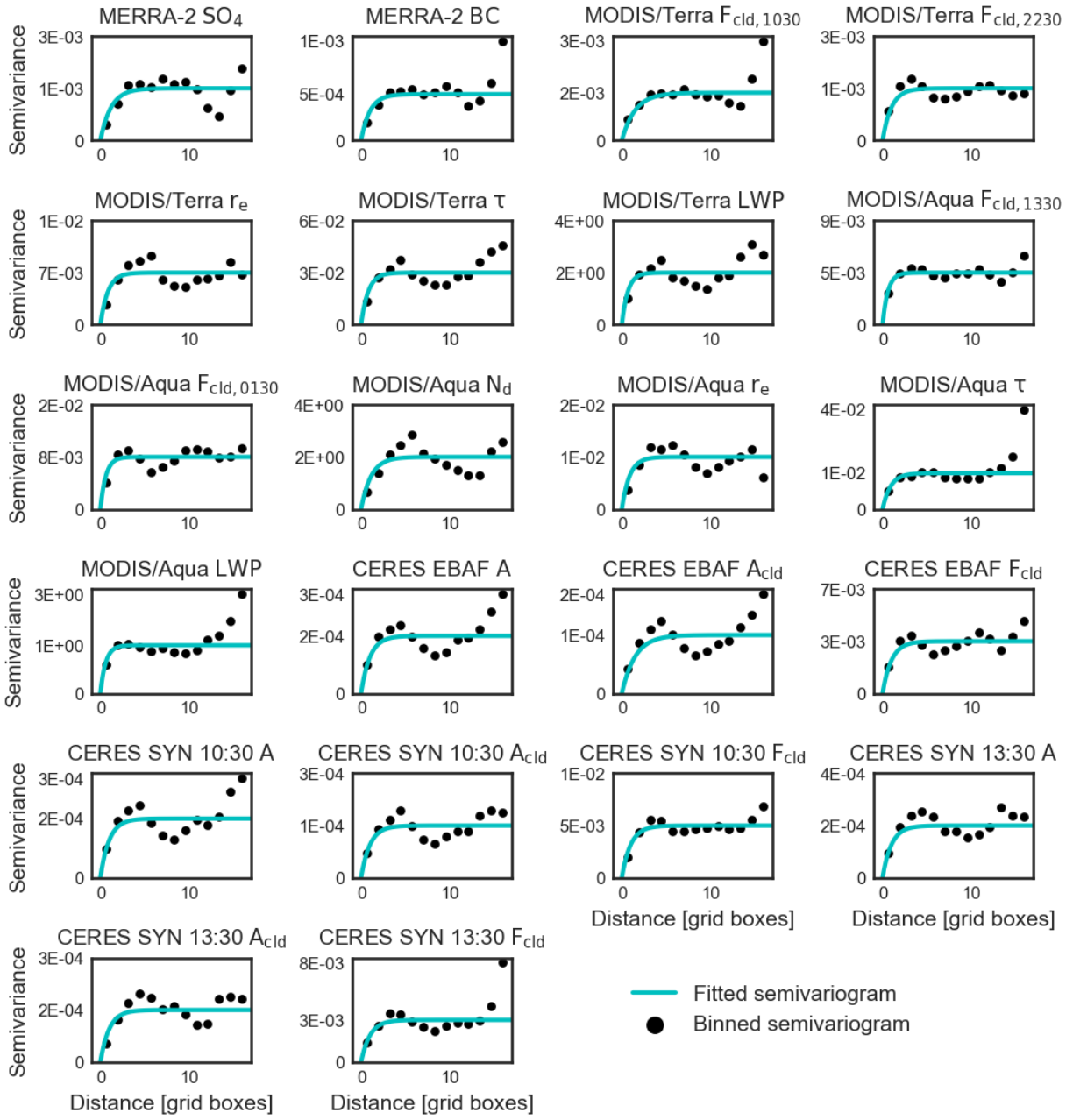

Figure S1. Semivariograms for all variables analyzed for the subtropical domain. The parametric (exponential) covariance model is fitted using weighted least squares.

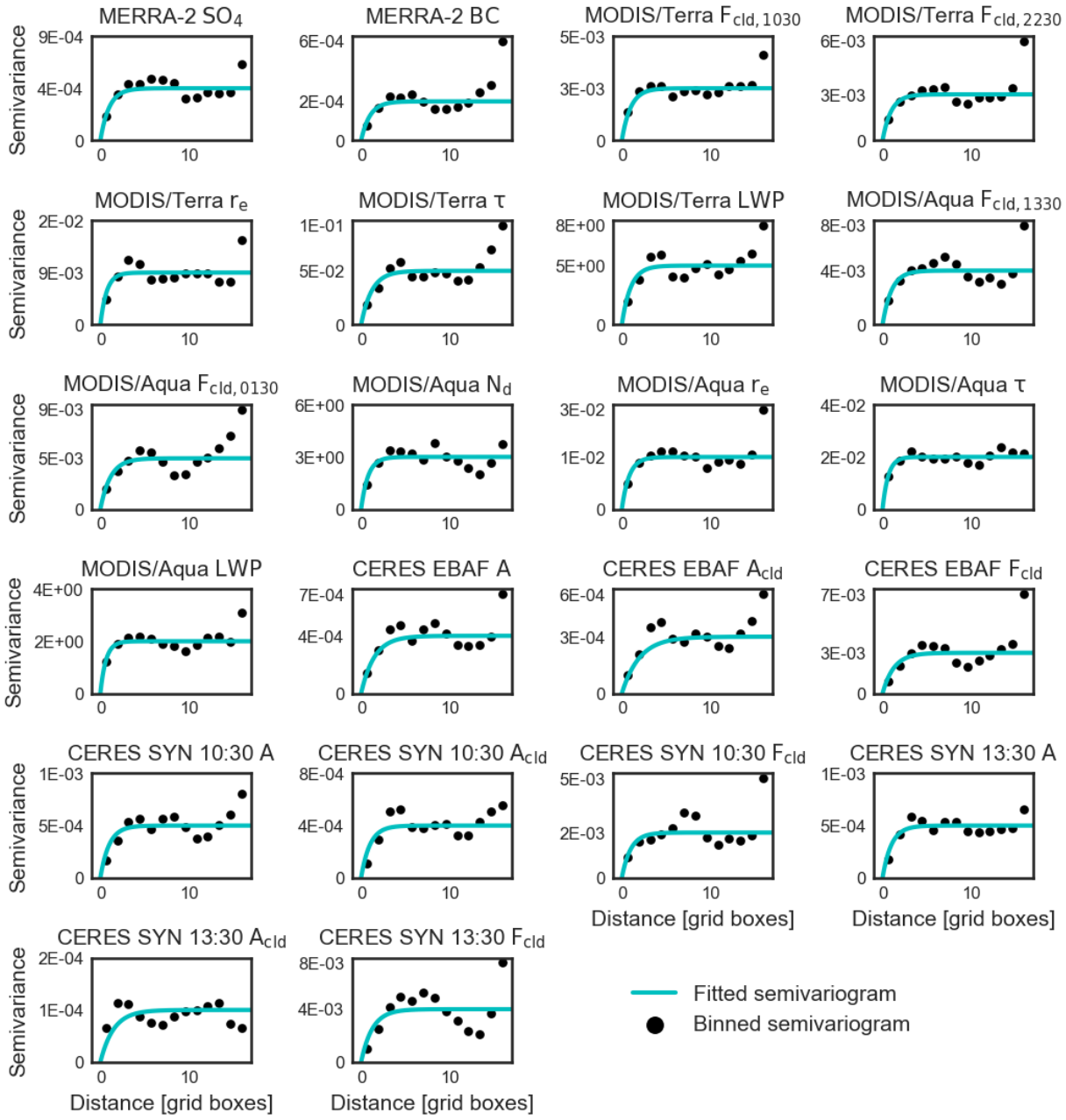

Figure S2. Semivariograms for all variables analyzed for the tropical domain. The parametric (exponential) covariance model is fitted using weighted least squares.

Modeling center	Model name	Number of ensemble members	Data citation
Beijing Climate Center (China)	BCC-ESM1	3	Beijing Climate Center (2018)
Centre National de Recherches Meteorologiques (France)	CNRM-ESM2-1	3	Seferian (2018)
Geophysical Fluid Dynamics Laboratory (United States)	GFDL-CM4	1	Guo et al. (2018)
	GFDL-ESM4	1	Krasting et al. (2018)
Institute for Numerical Mathematics (Russia)	INM-CM4-8	1	Volodin et al. (2019a)
	INM-CM5-0	8	Volodin et al. (2019b)
Japan Agency for Marine-Earth Science and Technology (Japan)	MIROC-ES2L	3	Hajima & Kawamiya (2019)
Met Office Hadley Centre (United Kingdom)	HadGEM3-GC31-LL	4	Ridley et al. (2019)
	UKESM1-0-LL	7	Tang et al. (2019)
National Center for Atmospheric Research (United States)	CESM2	14	Danabasoglu et al. (2019)
	CESM2-WACCM	3	Danabasoglu (2019)
NorESM Climate modeling Consortium (Norway)	NorESM2-LM	3	NorESM Climate modeling Consortium (2018)

Table S1. Modeling centers, model names, number of ensemble members available, and references for all of the CMIP6 models used.

Variable	Regressors used	Transformation	N_{sig}
MERRA-2			
Black carbon (BC)	LTS, lon, lon^2, lat^2, lat*lon	log	33
Sulfate (SO_4)	LTS, lon^2, lat, lat^2	log	38
MODIS/Terra			
Daytime cloud fraction ($F_{cld,1030}$)	EffLTS, lon, lon^2, lat	logit	0
Nighttime cloud fraction ($F_{cld,2230}$)	EffLTS, LTS, lon, lon^2, lat^2, lat*lon	logit	1
Effective radius (r_e)	EffLTS, lon, lat^2, lat*lon	none	25
Cloud optical thickness (τ)	EffLTS, LTS, lon, lon^2, lat, lat^2, lat*lon	none	1
Liquid water path (LWP)	EffLTS, LTS, lon, lon^2, lat, lat^2, lat*lon	none	0
MODIS/Aqua			
Daytime cloud fraction ($F_{cld,1330}$)	EffLTS, LTS, lon, lon^2, lat, lat^2	logit	0
Nighttime cloud fraction ($F_{cld,0130}$)	EffLTS, LTS, lon, lon^2, lat, lat^2, lat*lon	logit	0
Cloud droplet number (N_d)	EffLTS, LTS, lon, lon^2, lat*lon	none	25
Effective radius (r_e)	EffLTS, lon, lat*lon	none	24
Cloud optical thickness (τ)	EffLTS, LTS, lon, lon^2, lat*lon	none	0
Liquid water path (LWP)	EffLTS, LTS, lon, lon^2, lat*lon	none	4
CERES EBAF			
Total albedo (A)	EffLTS, LTS, lon, lon^2, lat, lat^2, lat*lon	logit	5
Cloud albedo (A_{cld})	EffLTS, LTS, lon, lon^2, lat, lat^2, lat*lon	logit	11
Cloud fraction (F_{cld})	EffLTS, LTS, lon, lon^2, lat^2, lat*lon	logit	3
CERES SYN (09:30-11:30 UTC)			
Total albedo (A)	EffLTS, LTS, lon, lon^2, lat, lat^2, lat*lon	logit	9
Cloud albedo (A_{cld})	EffLTS, LTS, lon, lon^2, lat, lat^2, lat*lon	logit	15
Cloud fraction (F_{cld})	EffLTS, lon, lon^2, lat^2	logit	5
CERES SYN (12:30-14:30 UTC)			
Total albedo (A)	EffLTS, LTS, lon, lon^2, lat*lon	logit	0
Cloud albedo (A_{cld})	EffLTS, LTS, lon, lon^2, lat*lon	logit	2
Cloud fraction (F_{cld})	EffLTS, LTS, lon, lon^2, lat*lon	logit	1

Table S2. The regressors that minimized the BIC and were used as regressors for the mean function in the kriging implementation, the transformation (if any) applied to the variable during kriging, and the number of individually significant grid boxes (out of a maximum possible value of 40) used in the calculation of field significance (N_{sig}) for each variable analyzed in the subtropical region.

Variable	Regressors used	Transformation	N_{sig}[1]
MERRA-2			
Black carbon (BC)	LTS, lon^2, lat, lat2, lat*lon	log	13
Sulfate (SO_4)	EffLTS, LTS, lon, lon^2, lat, lat^2, lat*lon	log	37
MODIS/Terra			
Daytime cloud fraction ($F_{cld,1030}$)	EffLTS, lon, lat, lat^2, lat*lon	logit	4
Nighttime cloud fraction ($F_{cld,2230}$)	lon, lon^2, lat^2, lat*lon	logit	2
Effective radius (r_e)	EffLTS, lon, lon^2, lat^2, lat*lon	none	5
Cloud optical thickness (τ)	lon^2, lat, lat^2	none	0
Liquid water path (LWP)	EffLTS, lon, lon^2, lat^2, lat*lon	none	0
MODIS/Aqua			
Daytime cloud fraction ($F_{cld,1330}$)	lon^2, lat^2, lat*lon	logit	7
Nighttime cloud fraction ($F_{cld,0130}$)	EffLTS, LTS, lon, lon^2, lat^2, lat*lon	logit	3
Cloud droplet number (N_d)	lon, lat, lat^2, lat*lon	none	6
Effective radius (r_e)	EffLTS, lon, lon^2, lat, lat^2, lat*lon	none	0
Cloud optical thickness (τ)	lon^2, lat, lat^2	none	1
Liquid water path (LWP)	EffLTS, lon, lon^2, lat^2, lat*lon	none	1
CERES EBAF			
Total albedo (A)	EffLTS, lon, lon^2, lat*lon	logit	4
Cloud albedo (A_{cld})	EffLTS, LTS, lon^2, lat^2, lat*lon	logit	2
Cloud fraction (F_{cld})	LTS, lon^2, lat^2, lat*lon	logit	4
CERES SYN (09:30-11:30 UTC)			
Total albedo (A)	EffLTS, LTS, lat, lat^2, lat*lon	logit	7
Cloud albedo (A_{cld})	EffLTS, lon, lat^2, lat*lon	logit	2
Cloud fraction (F_{cld})	EffLTS, lon^2, lat, lat^2, lat*lon	logit	8
CERES SYN (12:30-14:30 UTC)			
Total albedo (A)	lon, lon2, lat	logit	1
Cloud albedo (A_{cld})	LTS, lon, lon^2, lat, lat^2, lat*lon	logit	4
Cloud fraction (F_{cld})	LTS, lon^2, lat^2	logit	4

Table S3. The regressors that minimized the BIC and were used as regressors for the mean function in the kriging implementation, the transformation (if any) applied to the variable during kriging, and the number of individually significant grid boxes (out of a maximum possible value of 40) used in the calculation of field significance (N_{sig}) for each variable analyzed in the subtropical region.